

Research paper

A depth-averaged SPH study on spreading mechanisms of geophysical flows in debris basins: Implications for terminal barrier design requirements

George Robert Goodwin^{a,b}, Clarence Edward Choi^{b,*}

^a Université Grenoble Alpes, INRAE, ETNA, Grenoble, 38000, France

^b University of Hong Kong, Pokfulam, Hong Kong SAR, PR China



ARTICLE INFO

Keywords:

Landslides
Spreading
Debris basin
Barrier design
Smoothed particle hydrodynamics

ABSTRACT

Conservative estimates of forces from debris flows on barriers are computable using the ‘free field approach’, assuming that flows are channelised until impact. However, this approach neglects the reduced flow velocity and depth due to lateral spreading in basins, which depends on flow type. In this study, physical dam-break tests using (i) water and (ii) dry sand running out onto an unconfined planar surface are performed, and then used to evaluate rheological models coded into a depth-averaged SPH program. A numerical parametric study on material type, material volume, channel length (both affecting the Froude number Fr) and lateral confinement is then performed. For water, the spreading angle correlates with Fr and gives a conservative solution for impact force and spreading. Debris spreading depends on material volume and is thus scale-dependent. The internal strength of arrested debris enables obstacle formation, inhibiting downstream motion, and forcing higher volumes of oncoming material to flow laterally. Moreover, impact force requirements for terminal barriers could be reduced by >50 % when compared to 2D free-field flows, provided the barrier is placed sufficiently far downstream (>5 m). Three-dimensional analyses of flows entering basins should complement simplified two-dimensional analyses commonly adopted by engineers, potentially reducing overly-conservative designs.

1. Introduction

Channelised geophysical flows continue to be a hazard in mountainous regions around the world, and the risk posed by them is likely to increase due to anthropogenically induced changes in the climate (Froude and Petley, 2018). The solid volume fraction of channelised flows can vary greatly, from debris floods (which are dominated by viscous stresses) to debris flows (which are dominated by frictional stresses; see Iverson, 1997). To mitigate the hazard of such flows from impacting human settlements, barriers are often constructed (e.g. Mancarella and Hungr, 2010; Canelli et al., 2012; Vagnon et al., 2015; Kwan et al., 2016). In regions where space allows, these barriers may be constructed at the end of large ‘debris basins’ which primarily provide retention space for the flow materials (Johnson et al., 1991) (Fig. 1). These debris basins also allow geophysical flows to decelerate (de Linares et al., 2020) by making use of (i) energy-wasting processes within flows and (ii) lateral spreading to induce deceleration whilst overriding relatively flat terrain, causing debris fans in the process. (For commentary on debris fans, see Whipple and Dunne, 1992; Rickenmann, 2005; Berti and Simoni, 2007; Scheidl and Rickenmann, 2010; Michelini et al., 2017; Kang and Lee, 2018; de Haas et al., 2018).

As for barriers, impact loading from channelised flows have been well-studied (e.g. Faug et al., 2003, 2009; Gray et al., 2003; Pudasaini et al., 2007; Moriguchi et al., 2009; Mancarella and Hungr, 2010; Faug, 2015a, 2020; Ashwood and Hungr, 2016; Iverson et al., 2016; Leonardi et al., 2016; Ng et al., 2016; Albaba et al., 2018; Goodwin et al., 2021). This strong foundation of research has led to the development of detailed mathematical descriptions of the impact loading. For instance, for dry granular flows, Albaba et al. (2018) proposed an expression for the impact pressure, which can be re-framed in terms of the force per unit width on a barrier F/L :

$$\left(\frac{F}{L}\right) = h_1 \left[1 + \frac{1}{\left(\frac{\rho_2}{\rho_1} \cdot \frac{h_2}{h_1}\right) - 1} + \frac{1}{2Fr_1^2} \right] \rho_1 U_1^2 + \frac{1}{2} h_1 \left[\tan(\theta - \phi') \left(\frac{\rho_2}{\rho_1} \cdot \frac{h_2^2}{h_1^2}\right) \right] \rho_1 g h_1 \cos \theta \quad (1)$$

where h is the flow depth; ρ is the bulk flow density; g is acceleration due to gravity; U is the flow velocity; θ is the local channel inclination; ϕ' is an internal friction angle; and the subscripts ‘1’ and ‘2’ indicate

* Corresponding author.

E-mail addresses: cegeorge@hku.hk (G.R. Goodwin), cechoi@hku.hk (C.E. Choi).

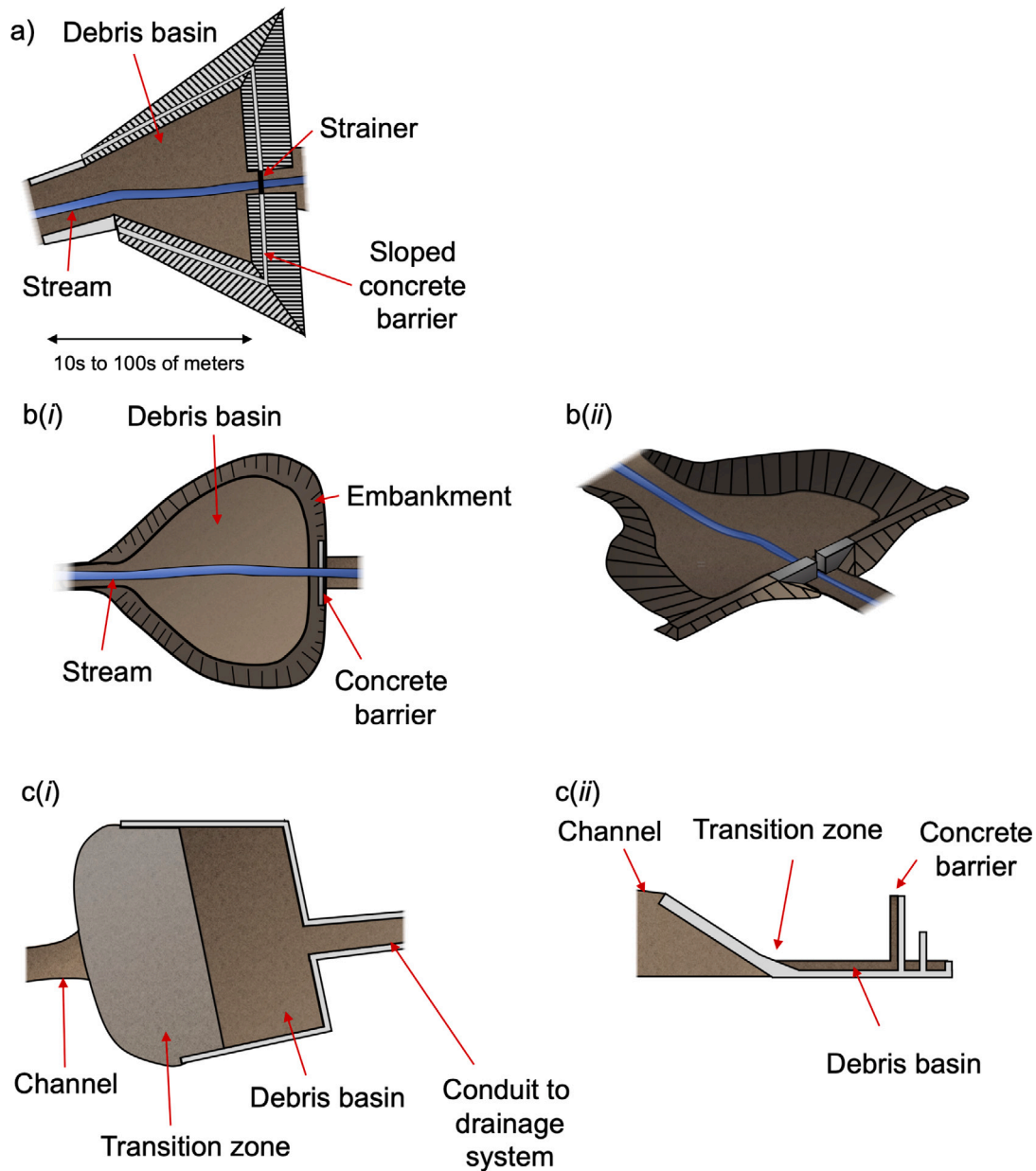


Fig. 1. A variety of debris basin configurations summarised from various sources. (a) Plan view of debris basin in Italy (redrawn from Cosenza et al., 2006 with an estimated length; (b) schematic debris basin: part (i), plan view, redrawn from Piton and Recking (2016); and part (ii), oblique view, redrawn from VanDine (1996); and (c) proposed debris basin from GEO (2008); part (i) is a plan view and part (ii) is a side-view cross-section. Other design details such as baffles or foliage are not included in the figure for clarity.

the flow before and after impact respectively. Fr is the Froude number, given by:

$$Fr = \frac{U}{gh \cos \theta} \quad (2)$$

The Froude number quantifies the ratio between inertial and gravitational forces for a channelised flow.

For practical purposes, however, simplified versions of equations such as Eq. (1) are used instead, disregarding the static component, and with most of the terms of the dynamic component condensed into an impact coefficient α :

$$\left(\frac{F}{L}\right) = (h) (\alpha \rho U^2) \quad (3)$$

Currently, it is still not yet practical for engineers to model the entire flow and impact processes explicitly within a single numerical program, given the extremely complex nature of debris flows. Equations with the same form as Eq. (3) are thus a simple solution for identifying

a likely upper bound for continuum-like flows. As such, practitioners often calculate the required resisting forces for barriers based on the calculated velocities and depths from 2D or 3D depth-averaged debris mobility models (e.g. Hungr, 1995; McDougall and Hungr, 2004; Kwan and Sun, 2006; Hungr, 2008; Iverson et al., 2010) near the point where a barrier is to be installed, rather than modeling the flow-barrier interaction explicitly.

The most conservative impact forces can be easily predicted using the 'free field approach'. This approach constitutes a two-dimensional plane-strain analysis. It assumes that the flow behaves as though it is channelised right up until and including impact. The free-field approach does not explicitly model flow-barrier interaction. Instead, it provides conservative estimates of the flow velocity and flow depth to calculate the design impact load.

However, this assumption crucially neglects the potential decrease in flow depth and velocity before impact due to lateral spreading in debris flow basins. Mechanically, lateral spreading causes momentum

to be directed away from the downstream direction, thus reducing the downstream velocity (Ng et al., 2013). It also causes the average flow depth to be reduced.

Although several investigations involving flow spreading have been conducted (e.g. Martinez, 2009; Ancey and Cochard, 2009; Jing et al., 2018; Kattel et al., 2018; Kafle et al., 2019), some specific features of the mechanics of spreading remain unclear. Indeed, phenomena complicating the matter further include: (i) time-varying earth pressure terms for granular flows (e.g. Hungr, 1995; McDougall and Hungr, 2004); (ii) the in-flux nature of Fr for transient flows (Ng et al., 2019); (iii) the influence of the volume of material, which is not well-correlated with runout length in field investigations (Rickenmann, 2005); and (iv) flow types dominated by different stresses. With regards to flow types, two important cases are: (i) debris flows which are dominated by frictional stresses (Iverson, 1997), and for which basal friction and varying earth pressure terms must be important for spreading; and (ii) debris floods, which are dominated by viscous stresses, and where earth pressures and basal friction are thus not relevant. Collectively, these effects make it difficult to assess how much the impact force per unit width on a terminal barrier could be reduced if the lateral spreading is accounted for in design.

2. Overview and objectives of this study

The most conservative impact forces can be easily computed using the ‘free field approach’, which assumes that the flow behaves as though it is channelised right up until and including impact. However, this assumption neglects any decrease in flow depth and velocity before impact due to lateral spreading in debris flow basins. The literature currently does not provide answers to how flow spreading links with upstream flow dynamics, nor how flow spreading can be accounted for when designing downstream barriers.

The main objective of this study is to assess the spreading behaviour of channelised flows as they enter a debris flow basin. The effects of spreading-related behaviour on the calculated impact force on barriers are then investigated and compared with the ‘free-field’ approach. We consider different flow rheologies, material volumes (both related to the pre-basin Froude number Fr) and degrees of lateral confinement in the debris basin.

Physical tests using (i) water and (ii) dry sand are performed using a laboratory-scale model developed for this study that allows initially channelised materials to spread out on an unconfined planar surface. Results from these tests, as well as well-established analytic solutions, are used to are then used to evaluate both fluid and frictional flow rheologies in a depth-averaged SPH model developed specifically for studying flows spreading in a basin. The model is then evaluated against a large-scale flume test involving wet gravel, recorded in the online USGS repository (Logan et al., 2018).

The SPH model is then used for a parametric study on material type, material volume ($2.5 < V < 30 \text{ m}^3$), channel length (affecting the Froude number Fr) and the degree of lateral confinement (with both quasi-2D and quasi-3D analyses). The spreading angle and the predicted impact loading on a terminal barrier are studied. The results from the numerical study should be useful for understanding the fundamental mechanisms governing potential reduction factors for the impact force exerted on terminal barriers situated at the end of basins.

3. Physical tests

For the physical experiments, a new 3.5 m long physical model was developed for this study. The model comprises an upstream storage section and a short channel, and a downstream spreading zone. To create a spreading zone, a wooden board with a surface area of approximately $2 \times 2 \text{ m}$ was fixed on top of an aluminium frame (Figs. 2 and 3). A channelised section used for storing the material before dam-break was also placed on an aluminium frame, such that the base of this section was flush with the wooden board.



Fig. 2. Frontal view of the experimental apparatus used in the physical tests.

3.1. Instrumentation

A GoPro camera was placed above the board to record the outflow of material from the channel. A grid was superimposed on the board to enable the correction of fish-eye distortion and to enable an assessment of the extent of lateral spreading of the flows. Correction of fish-eye was done manually for each frame using distortion-related features of the open-source photo-editing software GIMP (‘GNU Image Manipulation Program’). Furthermore, a single ultrasonic sensor was used to measure the depth of the flow. The ultrasonic sensor was placed in line with the centre of the channel, 1 m downstream from the gate.

3.2. Physical test procedure

The flow material was placed inside the storage section at the beginning of each test. The volume of the material was 0.024 m^3 for each case. The flume was then inclined to the desired angle using a manual fork-lift device; this angle was 5° for the water test and 34° for the sand test. The instrumentation was then activated. Finally, the gate was opened pneumatically, allowing the material to flow downstream into the channel, and then onto the board.

3.3. Test plan

The water was dyed blue using food colouring to make the spreading behaviour easier to observe.

For the dry sand test, Fraction C Leighton Buzzard sand (LB-C) was adopted. The nominal diameter of the LB-C sand was 0.3 to 0.6 mm (Choi et al., 2014, 2015a). The interface friction angle was determined from direct measurements obtained from a tilt-test, following the procedure outlined in Pudasaini et al. (2007), Mancarella and Hungr (2010) and Jiang and Towhata (2013). A cylindrical container with a diameter of approximately 20 cm, open at both ends, was filled to a depth of around 10 cm with dry sand. The container was then placed on the board forming the runout zone. Both the board and the flume were covered with the same transparent film to ensure a consistent basal friction angle. The board was gradually inclined until the cylinder started to move, at which point the inclination of the board was recorded. This procedure was repeated several times to characterise the error. The interface friction angle of both fractions of sand was measured to be around 22.6° , consistent with the measured basal friction reported by Choi et al. (2015b). A value of $\phi' = 32^\circ$ for all fractions of Leighton Buzzard sand was obtained in Cheuk et al. (2008), where ϕ' is the internal friction angle.

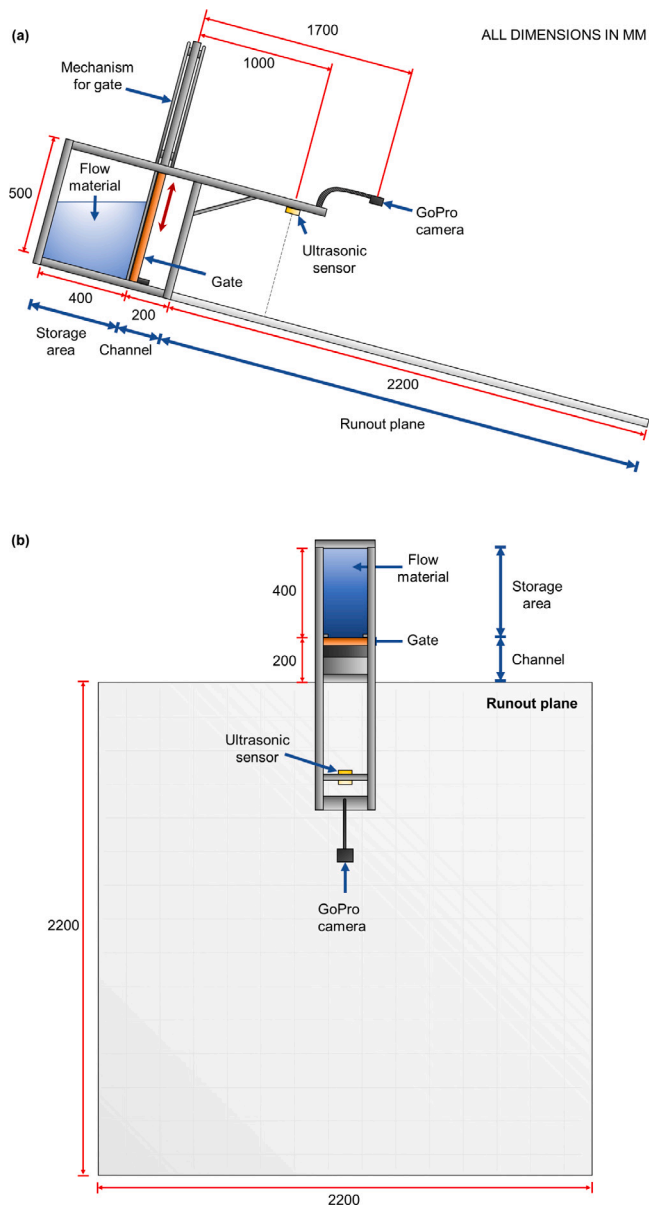


Fig. 3. Schematics of the experimental apparatus used in the physical tests. The dimensions were identical in the numerical simulations. (a) Side view; (b) plan view.

4. Numerical model: Depth-averaged smoothed particle hydrodynamics

4.1. Motivation for adopting the depth-averaged SPH

Before commencing the description of the depth-averaged SPH model developed and used in this study, we briefly justify its adoption in preference over other available numerical models. Indeed, we acknowledge the existence of other types of numerical model used for mechanically rigorous simulations of granular flows, including: (i) debris mobility models of the type presented in Hungr (1995) and Kwan and Sun (2006); (ii) the Discrete Element Method (e.g. Cundall and Strack, 1979; Favier et al., 2009; Salciarini et al., 2010; Law et al., 2015; Albaba et al., 2018; Leonardi et al., 2019); (iii) the Material Point Method (e.g. Abe and Konagai, 2016; Iaconeta et al., 2017); and (iv) D-CLAW (Iverson and George, 2014; George and Iverson, 2014). Also worthy of mention is the suite of statistical-empirical models which use empirical relationships to incorporate the effects of flow type into

flow-routing algorithms (e.g. Iverson et al., 1998; Huggel et al., 2003; Park et al., 2016; Kang and Lee, 2018).

The key advantages of the SPH (McDougall and Hungr, 2004; Laigle et al., 2007; Bui et al., 2008; Chambon et al., 2011; Crespo et al., 2015; Pastor et al., 2015, 2017, 2021) and MPM (Abe and Konagai, 2016) are that they allow the bulk constitutive behaviour of different rheologies to be computed relatively efficiently within a framework suitable for continuous large deformations (see Hungr, 2008). Modelling the basic constitutive behaviour improves insight into the mechanics of the flow and means that granular flows and viscous flows can be directly compared. Specifically, depth-averaged formulations give direct insight into earth-pressures and dissipative forces, which mechanically govern spreading, both laterally and longitudinally. Since simple depth-averaged SPH models are currently adopted in engineering practice (e.g. McDougall and Hungr, 2004; Kwan and Sun, 2007), we adopt the SPH in this study.

4.2. SPH governing equations

In this study, a simple depth-averaged SPH program was coded in MATLAB. The program is similar to those used in engineering practice (e.g. McDougall and Hungr, 2004). The basic underlying assumptions of the SPH as applied to flow-like landslides are: (i) the flow depth is small compared to the plan-view area of the flow; (ii) the flow material is incompressible; and (iii) that no external stresses act on the free surface of the flow (McDougall and Hungr, 2004). It is worth noting that some of the assumptions of the depth-averaged model are not strictly adhered to in the simulations. For instance, even though the derivation of the shallow-water equations assumes that the length of the flow is large compared to the depth, this is not the case initially, before dam-break occurs. A corollary of this assumption is that vertical velocity of the equivalent fluid can be ignored for the purposes of developing the depth-averaged equations. However, during dam-break, the vertical velocity of the flow front is not initially negligible. In the case of the depth-averaged SPH, this amounts to neglecting the influence of the vertical momentum component on the development of the flow, tending towards the development of downstream momentum that is higher than a fully 3D model might predict — although this superficially tends to the side of conservativeness.

In any case, this simplified model of momentum transfer is unlikely to be a governing source of error, since the initial downstream momentum only occurs at the very start of the flow, essentially just as it is entering the channel. Comparisons between analytic solutions and model output given later on in this manuscript (see Figs. 8 and 11) suggest that the effects of vertical momentum are extremely limited. In any case, any influence due to neglecting vertical momentum is likely small compared to the limitations intrinsic to dam-break scenarios themselves (see for instance Iverson and George, 2019). Indeed, most debris flows and landslides evolve from static masses of material, with initial movement starting from small perturbations from static equilibrium, although currently few industrially-feasible numerical approaches exist for capturing the true coupled hydromechanical initiation mechanisms. It should be emphasised that modelling techniques such as physical dam-break scenarios or numerical depth-averaged methods are primarily a means towards developing flows which are convenient and reproducible, and that there is a wide array of literature adopting these techniques (e.g. Hungr, 1995; McDougall and Hungr, 2004; Iverson et al., 2010; Salciarini et al., 2010; Jiang and Towhata, 2013; Iverson and George, 2014; Choi et al., 2015a), implying that they are acceptable tools for scientific investigation.

The depth-averaged SPH model described in McDougall and Hungr (2004) was used as the primary reference. Nonetheless, our model incorporates some key changes, notably in the implementation of kernel functions (partially following Solenthaler et al., 2011) and the way in which the boundaries are modelled for the channelised section.

The mass and momentum balances for the model are:

$$\frac{\partial h}{\partial t} + h \left(\frac{\partial U_x}{\partial x_x} + \frac{\partial U_y}{\partial x_y} \right) = 0 \quad (4)$$

$$\rho h \frac{\partial U_x}{\partial t} = \rho h g \cos(\theta_x) + k_x \sigma_z \left(-\frac{\partial h}{\partial x_x} \right) + k_{yx} \sigma_z \left(-\frac{\partial h}{\partial x_y} \right) + \tau_{zx} \quad (5)$$

$$\rho h \frac{\partial U_y}{\partial t} = \rho h g \cos(\theta_y) + k_y \sigma_z \left(-\frac{\partial h}{\partial x_y} \right) + k_{xy} \sigma_z \left(-\frac{\partial h}{\partial x_x} \right) + \tau_{zy} \quad (6)$$

where h is the flow depth; U_x and U_y are velocities in an orthogonal two-dimensional space; g is gravitational acceleration; θ_x and θ_y are the topographical inclinations on a two-dimensional plane, relative to the horizontal; k_x , k_y , k_{xy} and k_{yx} are stress ratios; and τ_{zx} and τ_{zy} are resisting shear forces that act on the base of the flow. The values of k_x and k_y are calculated at each time step. The orientation of the coordinate system is chosen such that k_{xy} and k_{yx} are zero. σ_z is the stress which acts normal to the bed, and is given by:

$$\sigma_z = \rho h (g \cos \theta_{xy} + |U|^2 \kappa) \quad (7)$$

where θ_{xy} is the local inclination of the xy -plane; $|U|$ is the magnitude of the velocity of the points; and κ is the curvature of the basal topography normal to the bed (and is the inverse of the radius of curvature). The term $|U|^2 \kappa$ represents centripetal acceleration caused by the flow moving over curved terrain, and has the effect of enhancing the driving forces for spreading (due to pressure gradients), as well as simultaneously increasing basal resisting forces. As for the basal resisting terms τ_{zx} and τ_{zy} , in this study we adopt two separate rheological models: one for granular materials and one for viscous fluids. These are discussed later.

4.3. SPH solver: kernel functions

In the SPH, the total mass of the flow is divided equally between Q columns that are centred on points known as smoothed particles. Certain properties of the points can be interpolated across a specified area in space. Kernels are mathematical functions which can be used to facilitate interpolation based on weighted spatial averaging.

For the depth-averaged SPH model used in this manuscript, both the density ρ and the volume V of the columns corresponding to the smoothed particles is fixed. Each smoothed particle has a finite depth h , and for a single smoothed particle p , the depth is proportional to the volume ($h_p \propto V_p$). If there are other smoothed particles in the vicinity (subscripted q), the depth increases based on the number, volume and distance of the nearby columns:

$$h_p = \sum_{q=1}^Q V_q W_{pq} \quad (8)$$

where W_{pq} is a kernel function mediating interactions between points p and q . W_{pq} governs how quantities are sampled over smoothed points in a particular vicinity. The local depth gradient can be calculated by applying the gradient operator ∇ to W_{pq} on the right-hand side.

The local depth gradient can be calculated by applying the gradient operator to W_{pq} on the right-hand side:

$$\nabla h_p = \sum_{q=1}^Q V_q \nabla W_{pq} \hat{n} \quad (9)$$

where \hat{n} is a unit vector. A similar operation can be applied to the fluid viscosity term for the viscous flow rheology.

In the SPH, there is no need to use the same kernel for forces caused by different physical phenomena (Müller et al., 2003; Solenthaler et al., 2011), provided that each kernel function is normalised to unity, i.e.:

$$\int W(r) dr = 1 \quad (10)$$

where r is the spacing between points.

McDougall and Hungry (2004) adopted a two-dimensional Gaussian kernel for their simulations of flows:

$$W_{\text{Gauss}} = \frac{1}{\pi \ell^2} \exp[-q^2] \quad (11)$$

where q is given by the spacing between points divided by the kernel radius r_{pq}/ℓ . However, W_{Gauss} does not offer finite support. Furthermore, the first derivative ∇W_{Gauss} , (required for pressure gradient calculations) can lead to points clumping together unphysically, since ∇W_{Gauss} goes to zero near the centre of the kernel. As such, we instead adopt the three kernels given in Müller et al. (2003) and Solenthaler et al. (2011), adapted for one and two dimensions. These kernels have the additional advantage of offering finite support, and avoiding potential issues with clumping. Normalisation constants Ω for kernels of one, two and three dimensions are calculated using the following relations:

$$\Omega_{1D} = \int_{-\ell}^{\ell} f(q) dq = 2 \int_0^{\ell} f(q) dq \quad (12)$$

$$\Omega_{2D} = 2\pi \int_0^{\ell} q f(q) dq \quad (13)$$

$$\Omega_{3D} = 4\pi \int_0^{\ell} q^2 f(q) dq \quad (14)$$

where $f(q)$ is the chosen kernel function. Note that the second and third of the above equations incorporate a circular surface integral and a spherical surface integral respectively. The final equation can be used to find the constants Ω given in Müller et al. (2003), which lead to the following expressions:

$$W_{\text{poly6 } 3D} = \frac{315}{64\pi\ell^3} (1 - q^2)^3 \quad (15)$$

$$W_{\text{spiky } 3D} = \frac{15}{\pi\ell^3} (1 - q)^3 \quad (16)$$

$$W_{\text{viscosity } 3D} = \frac{15}{2\pi\ell^3} \left(-\frac{q}{2} + q^2 + \frac{1}{2q} - 1 \right) \quad (17)$$

The leading normalisation coefficients for these three expressions were derived for a fully 3D case used in Müller et al. (2003); as such, the coefficients in the present paper are necessarily different. Furthermore, the derived forms used in this manuscript can be obtained by differentiation. It should be noted that for the depth-averaged method, a quasi-2D model requires a 1D kernel, whilst a quasi-3D model requires a 2D kernel. The appropriate derivatives of the three kernel functions that we implement for the quasi-2D cases are:

$$W_{\text{poly6 } 1D} = +\frac{35}{32\ell} (1 - q^2)^3 \quad (18)$$

$$\nabla W_{\text{spiky } 1D} = -\frac{2}{\ell^2} (1 - q)^2 \quad (19)$$

$$\nabla^2 W_{\text{visc } 1D} = +\frac{24}{\ell^3} (1 - q) \quad (20)$$

All three derivatives fulfil the condition of finite support, i.e. that the functions go to zero outside of the smoothing length ℓ to ensure numerical stability (Müller et al., 2003). Finally, for quasi-3D depth-averaged simulations of channelised flows, 2D kernel functions are required. The functions and derivatives adopted for the quasi-3D simulations were:

$$W_{\text{poly6 } 2D} = +\frac{4}{\pi\ell^2} (1 - q^2)^3 \quad (21)$$

$$\nabla W_{\text{spiky } 2D} = -\frac{30}{\pi\ell^3} (1 - q)^2 \quad (22)$$

$$\nabla^2 W_{\text{visc } 2D} = +\frac{40}{\pi\ell^4} (1 - q) \quad (23)$$

It should be noted that the initial viscous kernel function depends on the number of dimensions. A comparison of the Gaussian, 'poly6' and 'spiky' kernels is shown in Fig. 4.

The smoothing length dictates how many smoothed points are included per kernel calculation. If the size of the simulation domain is comparable to the volume of material, a fixed smoothing length may be acceptable (e.g. the 3D simulations in Müller et al., 2003).

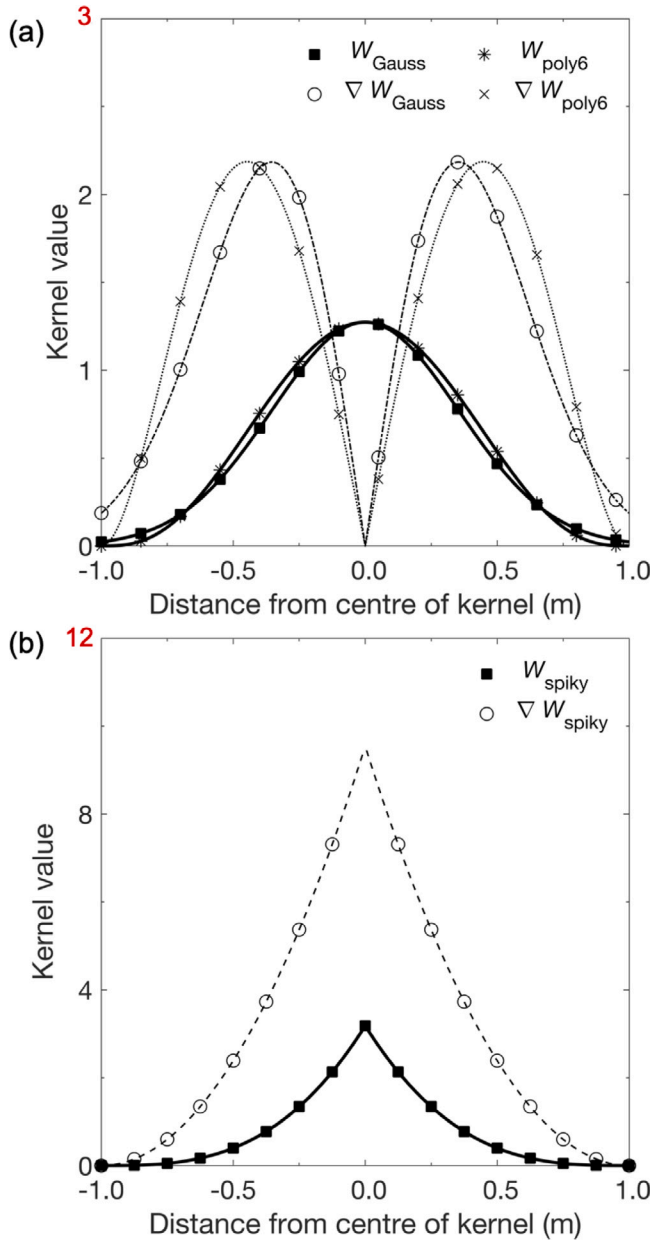


Fig. 4. Comparison of kernel types: (a) shows 2D Gaussian and 'poly6' kernels; (b) shows the 2D 'spiky' kernel. A nominal kernel radius ℓ of 1 is assumed for the 'poly6' and 'spiky' kernels, and 0.5 for the Gaussian kernel. The 'poly6' kernel reproduces the Gaussian kernel well, with the added advantage of finite support at the kernel edges. The kernel shapes and magnitudes for given values of ℓ are essentially identical for 1D and 2D cases.

In McDougall and Hungr (2004), however, an adaptive smoothing length was chosen, allowing the smoothing length to increase as the flow mass spreads out over a large domain.

Since this manuscript concerns flow spreading, we implement the same spatially-varying smoothing length function given in McDougall and Hungr (2004):

$$\ell_{1D} = \frac{BQ}{\sum_{q=1}^Q h_q V_q} \quad (24)$$

$$\ell_{2D} = \frac{B}{\sqrt{\frac{\sum_{q=1}^Q h_q V_q}{Q}}} \quad (25)$$

B is a dimensionless constant that approximately corresponds to the number of particles enclosed by the kernel in any given direction. Eqs. (24) and (25) effectively include a single average of the relative distances between smoothed points (since the height of each column h_q decreases as smoothed points move further apart). It should be noted that for the quasi-2D case, the term V is actually volume per unit width; whilst V is volume for the quasi-3D case.

4.4. Rheological models

4.4.1. Frictional materials: the Voellmy model

The model implemented for frictional materials is the Voellmy model (Hungr, 1995) which can be written as:

$$\tau_{zi} = \sigma_z \left(\tan \phi_b + \frac{|U|^2}{\xi} \right) \hat{n}_i \quad (26)$$

where i can be either the x or y direction; and ϕ_b is an effective basal friction angle. It is a function of the pore fluid pressure ratio r_b , according to $\phi_b = (1 - r_b) \tan \phi$, where ϕ is a dynamic basal friction angle (Hungr, 1995; McDougall and Hungr, 2004). The parameter ξ is called the 'turbulence coefficient' and is dimensionally equivalent to acceleration (Hungr, 1995). We interpret ξ as accounting for energy losses due to processes of internal dissipation such as frictional shearing, collisions between grains and air resistance (the latter applying to the back-analysis of the small-scale sand flow) (Choi and Goodwin, 2021). Finally, \hat{n}_i is a unit vector computed as $U_i/|U|$.

Special consideration must be given to the development of frictional forces whilst points are at rest (i.e. where $U_i = 0$). The maximum basal resisting force is given as follows:

$$\tau_{zi \max}|_{U_i=0} = \sigma_z (\tan \phi_b) \quad (27)$$

While points are at rest and have not yet reached the point of movement, the destabilising forces F_i are assumed to offset the current basal shear stress $\tau_{zi \text{ mob}}$:

$$F_i = - \left[\rho h g \cos(\theta_i) + k_i \sigma_z \left(-\frac{\partial h}{\partial i} \right) \right] \quad (28)$$

The resisting shear forces $\tau_{zi \text{ res}}$ are limited by F_i , and always oppose the direction of motion:

$$\tau_{zi \text{ res}}|_{U_i=0} = \begin{cases} -F_i & \text{if } \tau_{zi \text{ res}}|_{U_i=0} < \tau_{zi \max}|_{U_i=0} \\ \tau_{zi \max}|_{U_i=0} & \text{otherwise} \end{cases} \quad (29)$$

For frictional materials, the earth pressure coefficient, which dictates the rate at which the flow material spreads, must also be calculated. As smoothed points strain apart from each other, earth pressure is reduced, whereas if they move closer to one another the earth pressure increases.

In the present SPH formulation, strains for each point p are computed based on the displacements of other points q within the smoothing radius ℓ :

$$\Delta \epsilon_i = \sum_{q=1}^Q \frac{(x'_{i,pq} - x_{i,pq})}{x'_{i,pq}} \quad (30)$$

where $\Delta \epsilon_i$ is the change in the strain field for a series of points p in direction i ; $x_{i,pq}$ is the distance between points p and q in direction i ; and the dash (') indicates the value at the previous time step. The incremental earth pressure coefficient k_i can then be calculated:

$$k_i = k'_i + C \Delta \epsilon_i \quad (31)$$

where C is a dimensionless stiffness coefficient with a value set at $C = 200$ (McDougall and Hungr, 2004). It is assumed that the earth pressure in both directions is unity when the initial flow mass is at rest (as per Hungr, 1995; McDougall and Hungr, 2004).

The bounds of the earth pressures for the main direction of movement x are a function of the internal friction angle ϕ' and the basal

friction angle ϕ_{base} , and are given as follows (Iverson, 1997; McDougall and Hungr, 2004):

$$k_{x(\text{min/max})} = 2 \left[\frac{\pm \sqrt{1 - \cos^2 \phi' (1 + \tan^2 \phi_{\text{base}})}}{\cos^2 \phi'} \right] - 1 \quad (32)$$

In the cross-stream direction of movement j , the limits of the earth pressure coefficient are given as a function of the instantaneous value of k_i , and are thus updated each time step. Following (McDougall and Hungr, 2004):

$$k_{y(\text{min/max})} = \left[\left(\frac{k_x + 1}{2} \right) \pm \sqrt{\left(\frac{k_x - 1}{2} \right)^2 + \tan^2 \phi_{\text{base}}} \right] \left(\frac{1 \mp \sin \phi'}{1 \pm \sin \phi'} \right) \quad (33)$$

4.4.2. Viscous fluids: viscous model

The main difference between the viscous model and the Voellmy model is the way in which the term τ_{zi} is computed. A general expression for a Newtonian viscous fluid is:

$$\tau_{zi} = \mu \nabla^2 U_i \quad (34)$$

where μ is the dynamic viscosity of the fluid, ∇^2 is the Laplacian and U_i is a velocity term which can be symmetrised in different ways (see Liu and Liu, 2003; Müller et al., 2003). As noted by Müller et al. (2003), the viscosity forces depend on velocity differences (i.e. local shear rates) rather than the actual velocities. As such, the calculation of the viscosity term for an incompressible fluid is symmetrised as follows:

$$\tau_{zi,p} = \mu \sum_{q=1}^Q V_q (U_{i,q} - U_{i,p}) \nabla^2 W_i \quad (35)$$

It should be noted that for the viscous fluid rheology, the pressure ratios k_i and k_j that appear in Eq. (5) are both set to constant values of unity.

4.5. Boundary conditions for storage container & channel and input parameters

One of the key issues that this study seeks to address is the effects of the initial degree of channelisation on the downstream spreading of the flow materials. It is therefore necessary to implement a method of confining the material in the channel.

Two methods are used together: (i) a variant on the 'ghost particles' method used in other studies (e.g. Bui et al., 2008; Chambon et al., 2011; Vela Vela et al., 2019) and (ii) periodic boundaries (see Law et al., 2015; Jonsson et al., 2016; Ni et al., 2016).

A regular square lattice of ghost particles is generated at the front and back of the storage area to form a back-wall and a gate, both of which have a width B_{ch} . Most properties of the ghost particles are fixed in time and space. The ghost particles are considered in calculations for smoothed particles whenever they fall within a smoothed particle's kernel radius. To enforce conservation of mass, it is necessary to make the wall width w greater than or equal to the smoothing length ℓ . Given the variable smoothing length adopted (see Eq. (25)), w was set empirically to $2\ell_{i=0}$.

The only property of the ghost particles which is allowed to change with time is their depth. The depth is proportional to the volume of the ghost particles (Eqs. (8) and (9)). At each timestep, the weighted average depth of only the smoothed particles within distance ℓ of the ghost grains is calculated and normalised, i.e.

$$h_{\text{ghost},p} = \frac{1}{\sum_{q=1}^Q W_{pq}} \left(\sum_{q=1}^Q h_q W_{pq} \right) \quad (36)$$

The volume of the ghost points is then updated:

$$V_{\text{ghost},p} = V_{\text{initial}} \frac{h_{\text{ghost},p}}{h_{\text{initial}}} \quad (37)$$

where V_{initial} is the original volume assigned to all smoothed and ghost particles, and h_{initial} is the original composite depth prescribed for the flow mass (which in practice is a summation of the flow depths of several individual points, as per Eq. (8)). These updated volumes for the ghost particles are used in kernel calculations for the smoothed particles (Eqs. (8) and (9)). The overall effect of this volume reduction for the ghost particles is for the back wall and gate to provide a reaction force that is equal and opposite to the pressure due to the flow material.

Periodic boundaries were adopted for the two sides of the flume (see Law et al., 2015; Jonsson et al., 2016; Ni et al., 2016). This choice neglects effects due to boundary shearing. In fact, boundary effects have always been difficult to deal with rigorously using SPH models (e.g. Müller et al., 2003; Chambon et al., 2011; Crespo et al., 2015), and there is relatively little discussion of modelling boundaries for depth-averaged models in the open literature. This is why we chose to neglect any potential boundary shearing effects in our simulations, given that the main focus of this study is on lateral spreading in basins. The periodic boundaries were enforced by copying particles within the smoothing length distance of the two channel wall boundaries to outside the outer bounds of the opposite wall for the purposes of force calculations. Furthermore, points leaving one side of the channel were moved to the opposite side. It should be noted that this routine was applied only to particles within the channel: particles that had left the channel were no longer subjected to the periodic boundaries. The routine had the effect of stably maintaining cross-channel forces acting on the smoothed points until they had left the channel (see Fig. 5).

For time-stepping, a time interval of Δt is used for time integration of Eq. (5). The velocity of each smoothed point p is updated at each time step (McDougall and Hungr, 2004):

$$U_i = U'_i + \Delta t \left(\frac{\partial U_i}{\partial t} \right) \quad (38)$$

where $\partial U_i / \partial t$ is calculated from Eq. (5) for each smoothed point at each time step. The positions of the smoothed points are then updated with a central difference approximation to enhance numerical stability (McDougall and Hungr, 2004):

$$\Delta x_i = \frac{\Delta t}{2} (U_i + U'_i) \quad (39)$$

For all simulations, a variable time interval was adopted to strike a balance between computational time and computational stability. The time interval was adjusted at each time step based on the velocity of particles in the simulations and the distances between smoothed points:

$$\Delta t = \begin{cases} 1.1 \Delta t' & \text{if } \frac{\min(r_{pq})}{1/Q \sum_{p=1}^Q |U_p|} < \frac{\Delta t'}{2} \\ 0.5 \Delta t' & \text{otherwise} \end{cases} \quad (40)$$

4.6. Input parameters

The input parameters for the SPH model varied depending on the material being modelled. The only input parameters for water are the dynamic viscosity and the bulk density, which are well-established material parameters.

For the dry sand simulations, the internal friction angle was set following the physical measurements of the Leighton Buzzard sand given in Cheuk et al. (2008); whilst the interface friction angle was set following physical tilt tests in Choi et al. (2015c). The bulk density was set assuming a constant solid volume fraction of 0.6 and a material density of 2650 kg/m³ reported in previous studies (e.g. Choi et al., 2015c). The Voellmy coefficient ξ accounts for velocity-dependent energy losses, which could be caused by frictional shearing

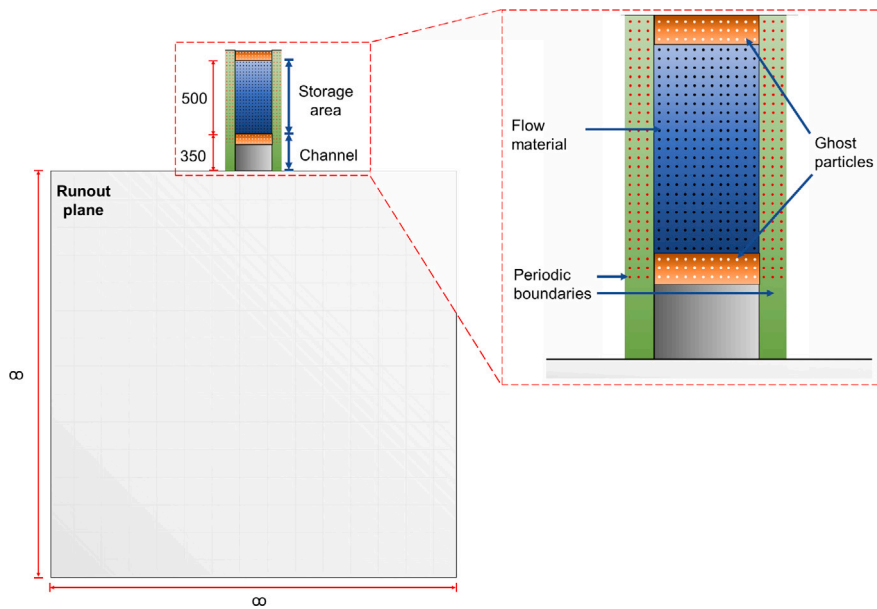


Fig. 5. Plan-view schematic of the numerical setup, including both periodic boundaries (shaded green with red points) and ghost particles (shaded orange with white points). Points constituting the flow are copied into the periodic zone only in the channel zone. The lower set of ghost particles constituting the gate are deleted after the flow material has reached equilibrium under the influence of gravity to simulate dam-break. The ghost particles and periodic boundaries are implemented in the same way for the SPH simulations using the USGS flume geometry: ghost particles are used for the back wall and the gate, whilst periodic boundaries are used all the way down the sides of the flume, up until the runout zone.

or collisions between grains. It has been established by Chalk et al. (2017) that the Voellmy coefficient is scale dependent; indeed, Chalk et al. (2017) found values of ξ on the order of 20 m/s^2 for small-scale flows. The value of $\xi = 12 \text{ m/s}^2$ in this study was obtained from tuning the parameter starting from the value given by Chalk et al. (2017) (see also Choi and Goodwin, 2021). The strain coefficient C for both the sand and debris cases was set at 200 following the value adopted in McDougall and Hungr (2004). The strain coefficient simply controls the rate at which the earth pressure can change depending on the strain; setting it at infinity simply means that the earth pressure reacts immediately to strain (McDougall and Hungr, 2004), jumping immediately to one of its boundary values, as in Gray et al. (1999).

For the debris, parameters such as the friction angles, the bulk density and the Voellmy coefficient of 500 m/s^2 were set following typical values given in design guidelines, which themselves are based on multiple back-analyses of field cases. (An excellent reference for such values is given in Kwan, 2012). With specific regards to the Voellmy coefficient, other studies have back-analysed values on a similar order of magnitude: Schraml et al. (2015) suggests ξ of 200 m/s^2 based on back-analyses of debris flow events. The strain rate coefficient was again set at 200 since strain is only indirectly a function of scale. As with the small-scale simulations, the value was able to give rise to non-instantaneous changes in the earth pressure at this scale, as intended, and was thus retained for the larger-scale simulations.

All of the properties are summarised in Table 1. These properties are summarised in Table 1.

5. SPH model evaluation

Evaluation of the depth-averaged Smoothed Particle Hydrodynamics (SPH) model is required to ensure that it can capture the key mechanisms relevant to the spreading of the flow material in field-scale basins. In this section, three comparisons are made: to the physical tests performed using the small-scale channel and spreading zone using (i) water and (ii) dry sand, and separately (iii) to a debris flow from one of the large-scale physical tests available from Logan et al. (2018). The value of the small-scale tests is that they are highly repeatable, have well-defined properties and do not include potentially confounding

Table 1

Input parameters for the calibration tests.

Material	Parameter	Units	Value
Water	Dynamic viscosity	Pa·s	0.001
	Bulk density	kg/m ³	1000
Sand	Internal friction angle	Degrees	32
	Interface friction angle	Degrees	22.6
	Bulk density	kg/m ³	1650
	Voellmy coefficient ξ	m/s ²	12
	Strain coefficient C	–	200
Debris	Internal friction angle	Degrees	40
	Interface friction angle	Degrees	39
	Pore pressure coefficient r_b	–	0.6
	Bulk density	kg/m ³	2000
	Voellmy coefficient ξ	m/s ²	500
Strain coefficient C	–	200	

mechanisms found in debris flows (e.g. consolidation and pore pressure diffusion). The water flow is used to evaluate the numerical model for viscous flows (which represent an upper bound for flow types dominated by viscous stresses such as debris floods), whilst the sand flow is used to evaluate the frictional rheological model. The value of the comparison with the debris flow test is to evaluate the limitations of the depth-averaged SPH model when applied to studying lateral spreading processes. It should be noted that the rheological model in this study for the sand and debris flows is the same; the only differences are the input parameters (including the back-analysed basal pore-pressure term r_b).

5.1. Idealised viscous flow (water)

Fig. 6 includes three components: a zoomed-in view of the physical test; the numerical depth-averaged SPH simulation; and a copy of the physical test, but scaled to be the same size as the screenshots of the numerical test. The channel inclination was 5° . Fig. 6a shows the physical test using water, at 5° . Fig. 6a(i) shows the flow at $t = 0.5 \text{ s}$ after dam break. The front of the flow has reached 0.8 m downstream from the start of the unchannelised zone. The sides of the flow have

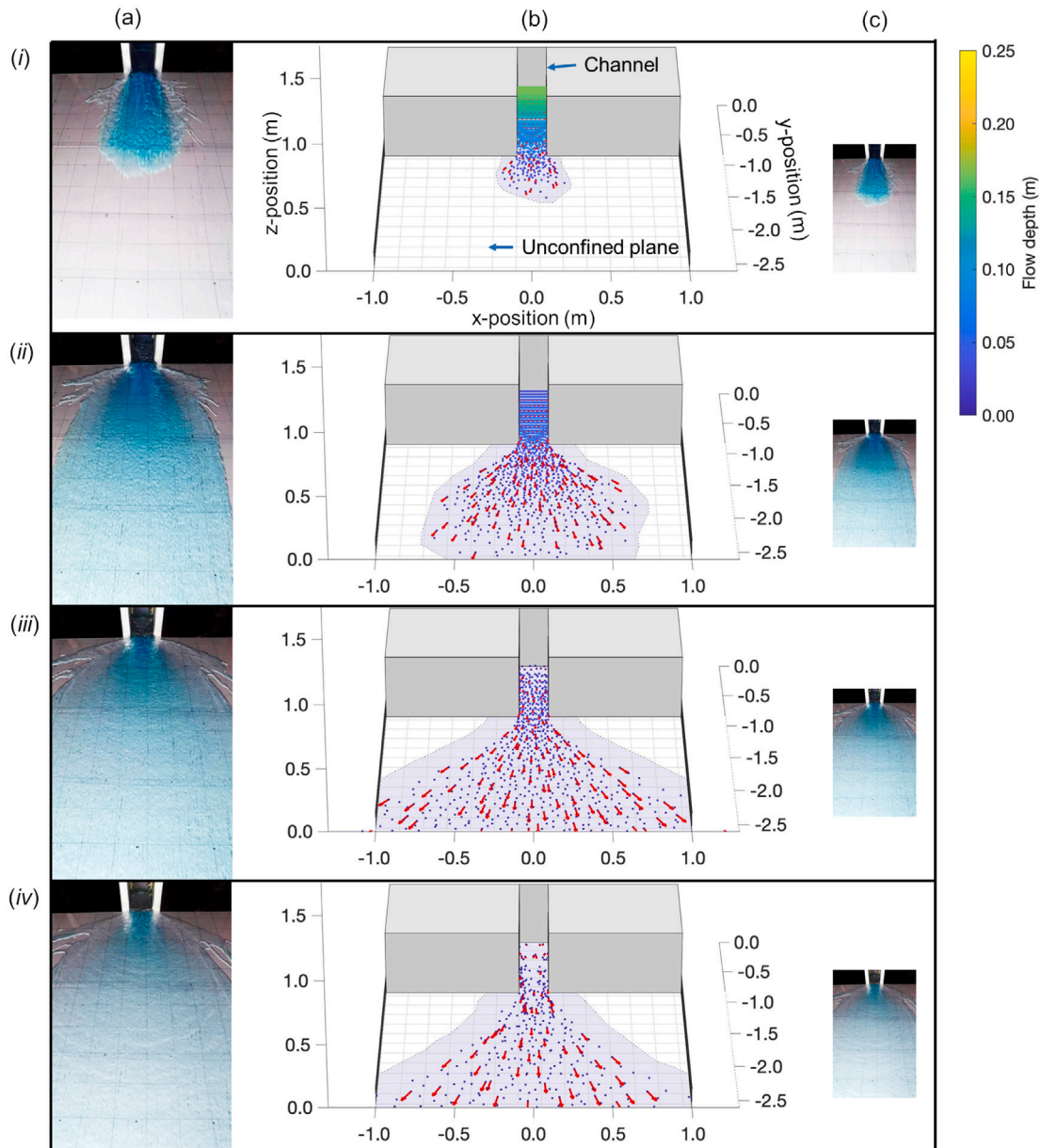


Fig. 6. Comparison between physical and computed flows. (a) Physical test using water on a 5° slope; (b) SPH back-analysis of the water case; (c) physical test scaled to be the same size as the numerical screenshots. The times for parts (i), (ii), (iii) and (iv) are $t = 0.5, 1.0, 1.5$ and 2.0 s respectively. For the SPH back-analyses, point colors correspond to the local depths. The shaded regions enclosed by dotted lines represent the bounds of the flow, including the smoothing length. The red vectors indicate the direction and magnitude of the velocity.

already started to spread laterally. Some fingering is observed on both sides near the upper end of the unchannelled zone, although this is not captured by the numerical model. At $t = 1.0$ s (Fig. 6a(ii)), the flow has reached the end of the unchannelled zone. The flow has spread laterally to a distance of about 0.5 m on each side of the bounds of the channel. At $t = 1.5$ to $t = 2.0$ s (Fig. 6a(iii) to iv)), in addition to flowing downstream, the flow increases the distance to which it spreads laterally.

Fig. 6b shows the numerical back-analysis of the physical water test. The overall trajectory of the flow downstream is similar to the physical test, reaching the same point downstream. The lateral spreading behaviour observed in the physical flow is also captured by the numerical simulation, with the observed spreading angle being similar for both cases. Fig. 7 shows a comparison of the physical and numerical depths. The physically measured depth is initially slightly higher than the computed depth; this can be attributed to the water being initially

turbulent, which is not modelled in the SPH. The quicker decrease of the flow depth for the SPH can be at least partially attributed to the surface tension of the residual water.

Fig. 8 shows another validation of the numerical model, by way of comparison with a 2D analytic model first presented in Ritter (1892), and later disseminated by Stoker (1957). This analytic model has previously been used for validating other SPH implementations, notably Wang and Shen (1999) and McDougall and Hungr (2004). The analytic model is derived from conservation of mass and momentum for a frictionless dam break, and gives the flow depth as a function of time:

$$h(x, t) = \begin{cases} h_0, & x < -c_0 t \\ \frac{h_0}{9} \left(2 - \frac{x}{c_0 t} \right)^2, & -c_0 t < x < 2c_0 t \\ 0, & x > 2c_0 t \end{cases} \quad (41)$$

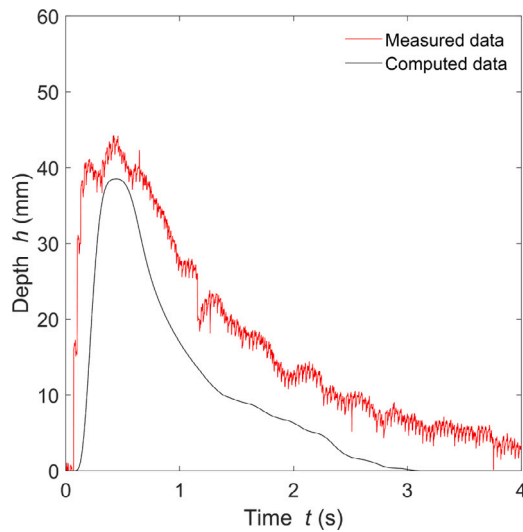


Fig. 7. Comparison between physical and computed flows: flow depths for water.

where x is position within a Eulerian coordinate system; h_0 is the initial height of the water in the dam; and c_0 is the speed of sound, which can be calculate as $c_0 = \sqrt{gh_0}$. For comparison with this model, the pseudo-2D SPH model was set up in a manner identical to McDougall and Hungr (2004), with 2000 smoothed points on a flat plane, a smoothing coefficient of $B = 10$ and an initial height of 10 m. The only difference compared to McDougall and Hungr (2004) is the kernel function employed, as has been discussed. Nevertheless, the match of the data from this model with the analytic model, and by extension McDougall and Hungr (2004), is excellent, thus validating the implementation of the Newtonian fluid model in the depth-averaged SPH model developed for this study.

It should be noted that there are two minor limitations of this implementation of the SPH for modelling fluid flows. First is the assumption of the averaged smoothing length across the entire flow. This leads to the apparent discontinuity just outside the mouth of the channel, where the outer bounds of the water flow (in terms of the outermost kernel radius) appear to go all the way to the upper edge of the unconfined plane. This could be addressed by defining independent smoothing lengths for each point. Secondly, surface tension forces become important for extremely shallow flows (including the fingering effects observed), and these are not captured in our SPH model. Surface tension forces are involved in the extent to which water spreads (see for instance Chengara et al., 2007), as well as the dynamics of water in general Müller et al. (2003). This is why the lateral spreading at $t = 1.0$ s (Figs. 6a(ii) and 6b(ii)) is overestimated slightly in the numerical model: the surface tension forces that tend to resist lateral spreading are not considered. Effects such as surface tension and turbulence are expected to slow flows, and it is thus expected that the model would give conservative results for large-scale flow cases.

5.2. Idealised frictional flow (dry sand)

Fig. 9a shows the physical test using dry sand, at 34° . Fig. 9b(i) shows the flow at $t = 0.5$ s after dam break. At $t = 1.0$ s (Fig. 9a(ii)), the flow has almost reached the end of the visible part of the unchannelised zone. At this point, the flow has undergone some lateral spreading to a distance of about 0.2 m further than the lateral bounds of the channel. Spreading increases slightly further down the unconfined plane. At $t = 1.5$ to $t = 2.0$ s (Fig. 9a(iii) to iv)), the flow continues to run out downstream.

Fig. 9b shows the numerical back-analysis of the physical sand test. The overall trajectory of the flow downstream is similar to the physical

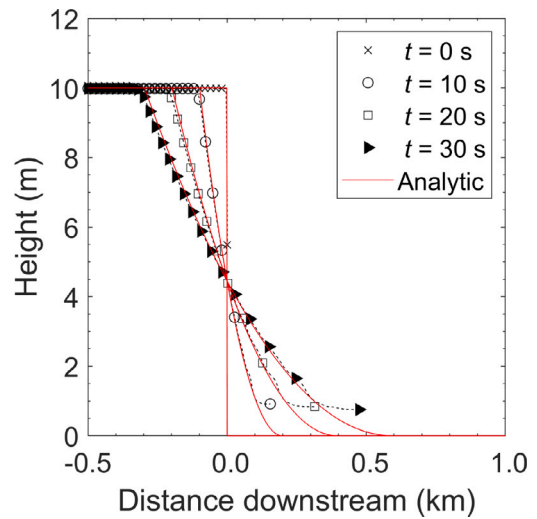


Fig. 8. Comparison between analytic and computed flows: flow depths for 2D water flows as a function of time and space.

test, in terms of the position of the flow front. Lateral spreading is captured by the model, as evidenced from Fig. 9b(ii) onwards, although the extent is perhaps slightly less than that observed in the physical test. This may be because of effects relating to air resistance, which are elevated at low confining stresses for sands (see Kessler et al., 2020), although tuning the Voellmy parameter ξ does account for some effects of air resistance indirectly.

Fig. 10 shows a comparison of the physical and numerical depths. The magnitude of the match is reasonable, although the physical measurements are somewhat unstable; this is attributed to the saltation of individual sand grains, which are not modelled in the depth-averaged SPH.

Fig. 11 shows a further validation of the ability of the numerical model to determine the evolution of the flow depth correctly. The SPH model is compared with a 2D analytic model presented in Mangeny et al. (2000), which is an extension of the model already presented from Ritter (1892) and Stoker (1957). The model by Mangeny et al. (2000) has been used for validating the frictional SPH model implemented in McDougall and Hungr (2004). The analytic model is derived from conservation of mass and momentum for a frictional flow undergoing dam break, and gives the flow depth as a function of time. This time, an extra parameter m_{Mang} is required to capture the effects of channel inclination and basal friction:

$$m_{\text{Mang}} = -g \sin \theta + g \cos \theta \tan \phi_b \quad (42)$$

where g is taken to be 9.8 m/s^2 . The development of the height of the flow can then be written in terms of a new constant, specifically $M = -\frac{1}{2}m_{\text{Mang}}t^2$:

$$h(x, t) = \begin{cases} h_0, & x < -c_0t - M \\ \frac{h_0}{9g \cos \theta} \left(2c_0 - \frac{x}{t} - M \right)^2, & -c_0t - M < x < 2c_0t - M \\ 0, & x > 2c_0t - M \end{cases} \quad (43)$$

To compare with this analytic model, the pseudo-2D SPH model was set up in a manner similar to that of McDougall and Hungr (2004), with 2000 smoothed points on an inclined plane, a smoothing coefficient of $B = 10$ and an initial height of 10 m. For our case, we adopted a basal friction angle of 32° and a channel inclination of 34° , to match the physical experiment. It should be noted that since the analytic model does not consider earth pressure, a constant value of $k_x = 1$ was adopted. The match between our SPH model and the analytic model by Mangeny et al. (2000) is very close. The slight differences are

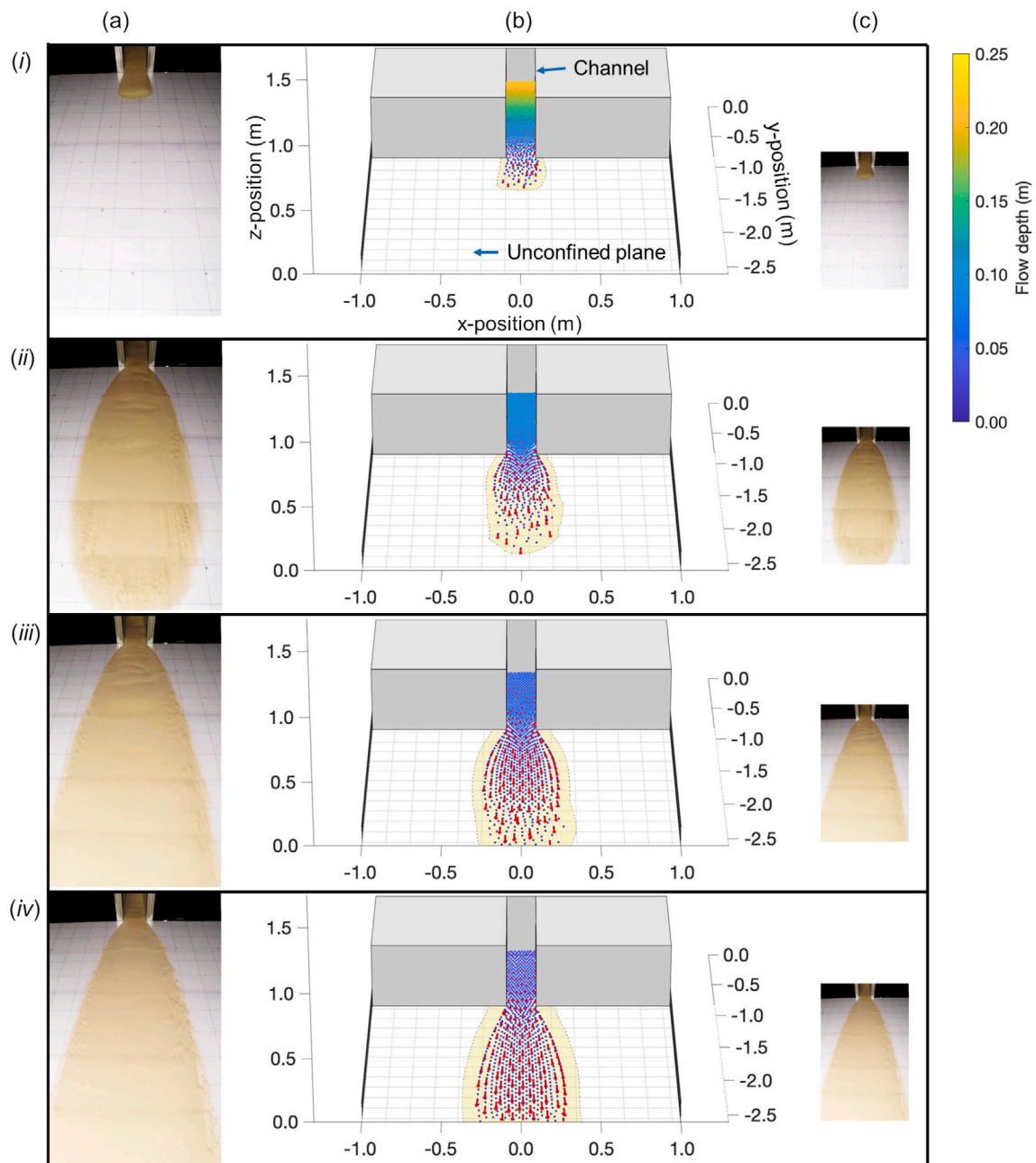


Fig. 9. Comparison between physical and computed flows. (a) Physical test using dry sand on a 34° slope; (b) SPH back-analysis of the sand case; (c) physical test scaled to be the same size as the numerical screenshots.

due to the fact that the finite volume ascribed to each smoothed point means that there is a minimum height that can be attained in the SPH (as discussed in McDougall and Hungr, 2004). This exercise further validates the implementation of the SPH in this study.

Nonetheless, Figs. 6 to 10 show that the two simple rheologies implemented in the SPH model produce reasonable descriptions of the physical behaviour observed, lending confidence to the application of the SPH model to other problems.

5.3. Debris flow

The final evaluation of the SPH model for capturing the relevant spreading mechanisms is based on data available from Logan et al. (2018) and Iverson et al. (2010). Iverson et al. (2010) details a flume and a runout zone with a combined length of over 100 m. The flume facility is one of the largest in the world with a complete database of

test data, which is ideal for model evaluation. The width of the channel is 2 m. A storage area at the top of the channel is where up to 10 m³ of debris material is placed before opening the gate to enable dam-break. Furthermore, there is a curvilinear transition between the channel and the runout zone.

The physical USGS channel is not entirely planar, with an imperfect cross-channel inclination of up to 1°. However, the 2° longitudinal inclination of the runout zone was considered, as was the transition between the end of the channel and the runout zone (modelled as an interpolated spline function in this study).

The frictional rheology that was evaluated in Section 5.2 was used, the only difference being the pore pressure coefficient. To speed up these simulations, the channelised part of the flow was modelled using the 2D depth-averaged implementation of the SPH model. The transition was implemented when the front of the flow reached the end of the channel. At this moment, the profile of the entire 2D flow,

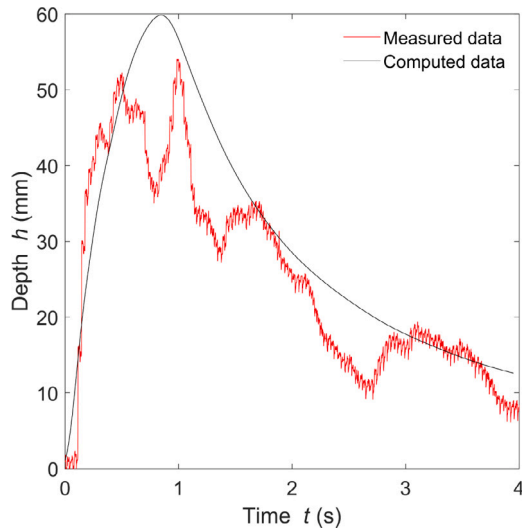


Fig. 10. Comparison between physical and computed flows: flow depths for sand.

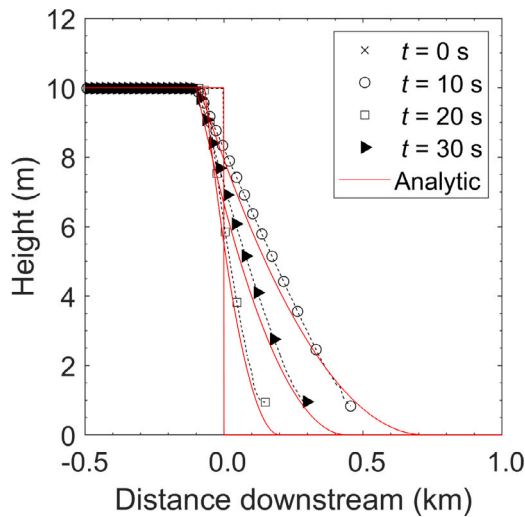


Fig. 11. Comparison between analytic and computed flows: flow depths for 2D frictional flows on an inclined plane, as a function of time and space.

including all of the material still within the channel was copied multiple times across the width of the channel. The spacing between “slices” was equal to the original spacing of points in the storage area. This copying process included all attributes for the particles, including the downstream velocity, the position, the downstream earth pressure, and so on. The property V of the points was adjusted to account for the transition from quasi-2D (where V is volume per unit width) to quasi-3D (where V is volume). Most of the cross-stream (y -direction) attributes were initialised to be zero, so that (for example) the initial cross-stream velocities and forces were initially zero. In contrast, the cross-stream earth pressures k_y were initialised at unity, and the upper and lower limits were initialised individually for each point based on the local downstream earth pressures k_x (see Eq. (33)). The final part of the transition to quasi-3D involved activating the periodic boundaries that were used to keep the flow channelised (see Fig. 5).

It should be noted that the conditions for modelling the USGS flume were complicated due to there being two basal friction coefficients: one for the storage container and runout zone, and another one for the channel. These were implemented as separate sections, and the bounds for the earth pressure coefficients were calculated separately on each section. Finally, the number of smoothed points for this particular case

was around 1500, corresponding to around 20,000 points for a full 3D simulation. The number of points for simulations with larger volume of material was up to around 4,500, corresponding to around 60,000 points for a full 3D simulation. The model is shown in Fig. 12.

The large-scale case adopted for comparison with the numerical model involved wet Steilacoom gravel. The test took place on 12th September 1995; video recordings of the test are freely available on the online USGS repository (Logan et al., 2018). The time taken for the flow front to reach the downstream mouth of the channel was captured well by the numerical model — both took around 10 s. The numerical case in this study adopted r_b to be set to 0.6. This value corresponds to a constant hydrostatic pressure from water within the flow where the water table is a little below the surface for the chosen bulk density (2000 kg/m^3). This value was obtained from calibrating the position of the flow front between the physical and numerical parts of the study. We nonetheless acknowledge that treatments do exist for modelling dynamic pore pressures Iverson (2005) and Pastor et al. (2015, 2021); there would be considerable value in exploring the effects of dynamic pore pressures on lateral flow spreading in basins in the future.

Indeed, a dynamic value of r_b may be able to match the simulation results by accounting for the changes in the excess pore pressures that occur during flows Iverson (2005). In particular, as the flow starts to come to rest, to the desaturation of highly permeable flow material occurs (see the videos relating to “wet gravel” and “beach sand” included in the USGS video repository; Logan et al., 2018). Indeed, if all smoothed nodes are assumed to act independently, from each other, the one-dimensional groundwater equation can be used to solve the diffusion of pore pressure within the soil mass:

$$\frac{\partial p_w}{\partial t} = D \frac{\partial^2 p_w}{\partial z^2} \quad (44)$$

where p_w is the local pore pressure and D is a diffusion coefficient which can be formed constitutively. By setting appropriate boundary conditions, rainfall infiltration, drainage and changes in pore pressure due to dilation/contraction can be modelled Iverson (2005). Nonetheless, for simplicity, the model used in this study was limited to a constant value, as per studies such as McDougall and Hungr (2004).

Fig. 13 shows comparisons of the position of the deposit of the same flow with respect to a wet gravelly flow, videography of which is available online (see Logan et al., 2018). The images were obtained by using screen captures. (Fig. 13b) was manually adjusted using the software GIMP to eliminate fish-eye, using the grid on the base of the channel as a reference; the image was also rotated, and the timestamp (originally superimposed over the mixture of water and fines) was airbrushed out for clarity. (Fig. 13b) is the final frame in the video for the top-down view. The frames in (Fig. 13c) show the final deposition from different angles; these images were brightened and sharpened using GIMP, to improve the original VHS images.

The overall deposition areas of the computed case (Fig. 13a) and the physical case (Fig. 13b) are similar. The peak of the physical deposition is similar to the peak of the computed deposition; this can be verified by inspecting the screengrabs collected in part (c). Furthermore, both the physical and computed results include spreading of the flow; Fig. 13c(iii) shows that the flow material can be found to the sides of the channel mouth. One difference between the physical and computed results is that the physical deposition includes a thin frontal layer of gravel, which is a consequence of the gravel moving discretely, and thus not being in constant contact with the base of the runout zone. This means that the retarding forces are limited for this frontal spray of gravel; it is well-established that continuum mechanics are not able to capture this type of discrete behaviour (Ng et al., 2017; Choi and Goodwin, 2021). One other difference is the strong asymmetry of the deposits from the physical test; this is due to the slight lateral tilt of the flume (see Fig. 12c), which is not considered in our numerical simulations.

A comment on ‘rheologies’ should also be made: for prototype debris flows, Iverson (2003) points out that ‘rheologies’ are of limited

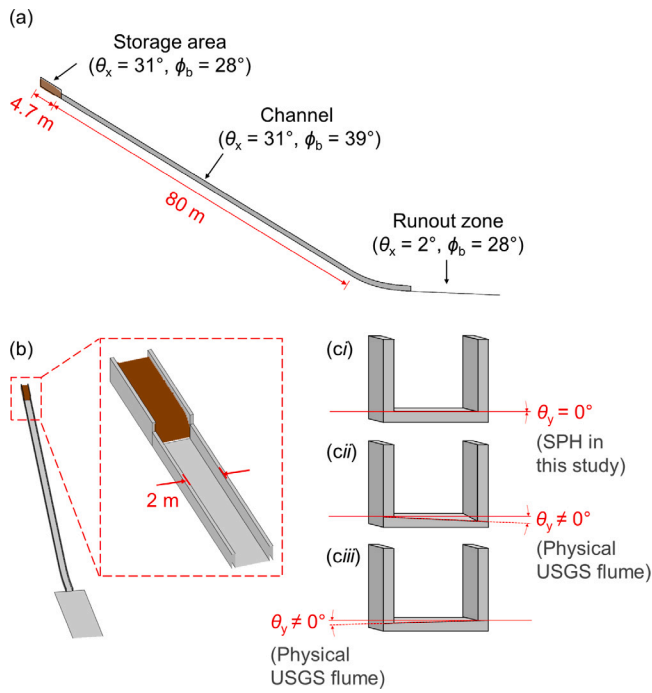


Fig. 12. The numerical model of the back-analysis for the test from Iverson et al. (2010), rendered in MATLAB. (a) Side view; (b) oblique view; (c) upstream view of the channel illustrating the lateral tilt present in the USGS flume: (i) no lateral tilt (adopted for the entire flume in this study); (ii) rightwards lateral tilt; (iii) leftwards lateral tilt. The latter two cases only affect the physical USGS flume.

use since they cannot be static during outflow. Nonetheless, a static rheology is adopted in this study for simplicity, given that the depth-averaged SPH is intended to be an idealised and routine engineering tool. Finally, we acknowledge the existence of other debris flow rheologies (see for instance Whipple and Dunne, 1992; Hungr, 1995; Rickenmann et al., 2006), which may be studied in future research campaigns.

6. Interpretation of results

Having established that the rheologies for Newtonian liquids and frictional materials can adequately capture the phenomenon of lateral spreading, a parametric study is conducted in this section. The ultimate challenge for each material is to determine the possible reduction in design impact force on a hypothetical terminal barrier if lateral spreading is explicitly accounted for, as opposed to cases where lateral spreading is neglected. This topic merits investigation since current ‘free-field’ (2D) approaches neglect lateral spreading (e.g. Kwan, 2012).

6.1. Characterisation of the Froude number Fr

The geometry of the flume is based on the dimensions given in Iverson et al. (2010) and shown already in Fig. 12. The flume length is varied to control the entry Froude number $Fr = U / \sqrt{gh \cos \theta}$ (see FHA (Federal Highway Administration), 2006), whilst the initial volume of flow material is also varied. The Froude number indicates the ratio of inertial to gravitational forces (e.g. Hübl et al., 2009; Armanini et al., 2011, 2014; Armanini, 2015; Choi et al., 2015a; Faug, 2015b). As for the procedure for obtaining the Froude number along the length

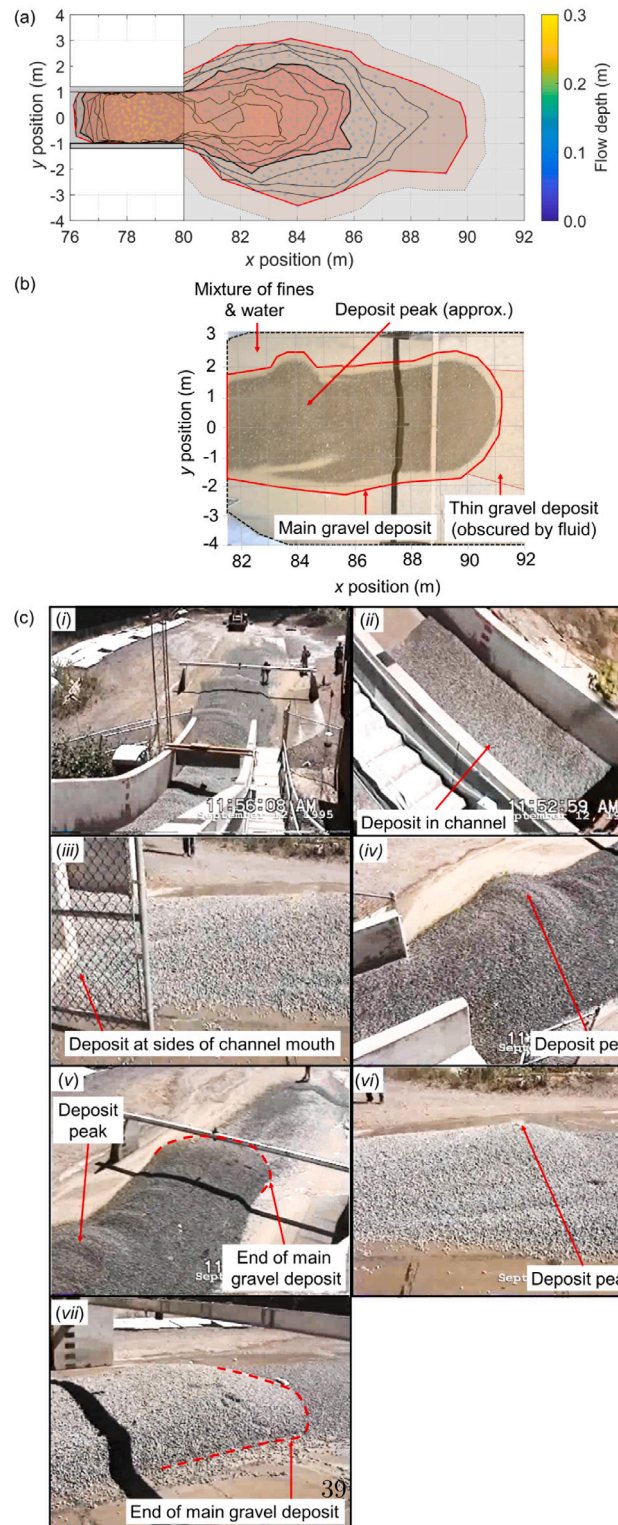


Fig. 13. Comparison of the SPH results from this study with the deposit from a gravel and water flow on a rough bed from Logan et al. (2018). Part (a) shows a plan view of the numerical results; part (b) shows a plan view of the physical results scaled to be the same size; part (c) shows a series of screengrabs showing the flow material after deposition has occurred.

of the flow, we adapt the procedure used in Ng et al. (2019) to the depth-averaged SPH (see also Goodwin and Choi, 2020; Goodwin et al., 2021). An average of the velocities and depths of smoothed points

within a monitoring region is used to calculate Fr :

$$Fr = \frac{\frac{1}{Q} \sum_{q=1}^Q U_q}{\sqrt{\frac{1}{Q} \sum_{q=1}^Q g h_q \cos \theta_q}} \quad (45)$$

This provides essentially identical results to sampling the local Fr using a kernel function. It should be noted that the local topography angle for each point θ_q needs to be accounted for given the curvilinear transition between channel and runout zone. The monitoring region is shown in Fig. 14a. The flow front and flow tail are also defined graphically.

Figs. 14b and 14c show the Froude profiles along the length of two different types of flow: a viscous Newtonian liquid (water), and debris, respectively. Fig. 14b shows that the Froude number for water increases approximately linearly along the entire length of the flow as the channel length is increased. The general trend of Fr being maximal at the front and minimal at the tail is consistent with flows of glass beads travelling down infinite slopes (Ng et al., 2019; Goodwin and Choi, 2020; Goodwin et al., 2021). In contrast, Fig. 14c shows that for debris flows, the frontal maximum value of Fr tends to increase with channel length. However, the increase is asymptotic: the increase between $L_{chan} = 20$ and 80 is minimal because flows tend to reach terminal velocity because of the Voellmy term ξ , which increases in magnitude as the velocity increases. Furthermore, unlike the water flows, Fr tends to decrease near the tail of the flow. This is because these flows tend to come to rest after exiting the channel, because the basal friction coefficient is higher than the inclination of the runout zone (which is set at 2°). For the flows on shorter channels ($5 < L < 20$ m), all of the flow material eventually exits the channel, which is why Fr has a non-zero value near the tail. For the flow on the longer channel ($L = 80$ m), the flow has dissipated its entire potential for longitudinal spreading (i.e. spreading in the downstream direction; (see also Ng et al., 2013)) by the time it reaches the end of the channel. (In other words, the driving forces due to the pressure gradient have reduced to almost zero.) Although the flow thickens slightly as it traverses the curvilinear transition, the increase in forces due to the pressure gradient are insufficient to drive the flow, so Fr tends to zero.

The difference in magnitude between the Newtonian liquid and debris flows should also be noted. For the same channel length, Fr is between two and six times higher for the Newtonian liquid than for debris. This is indicative of the high levels of energy dissipation due to the Voellmy terms ϕ_b and ξ for the debris flow model. Although the values of Fr for the Newtonian liquid are considered to be an upper bound since turbulence is not considered, Fr for these water flows is expected to remain much higher than the debris flows even if dissipative effects due to turbulence were considered.

Due to the fundamentally different shapes of the Fr profiles along the lengths of these unsteady flows, we primarily use $Fr_{max} \equiv Fr_{frontal}$ when referring to the two types of flow throughout the remainder of the manuscript.

Finally, it should be noted that altering the volume of the flow material does not alter the overall trends for the Fr profiles using the sampling region adopted in this section (Fig. 14a). For both water and debris, Fr tends to decrease slightly with volume. This is because although there is more potential for longitudinal spreading forces to drive the downstream flow velocity, the flow tends to be substantially deeper. For conciseness, the Froude profiles for these cases are not shown, although values for Fr used in reference to such cases were extracted in the same way as described in this section.

6.2. Spreading angles

This section discusses the spreading angles of different types of flows. Although flow spreading in basins has received attention before (e.g. Whipple and Dunne, 1992; Rickenmann, 2005; Berti and Simoni, 2007; Scheidl and Rickenmann, 2010; Michelini et al., 2017; de

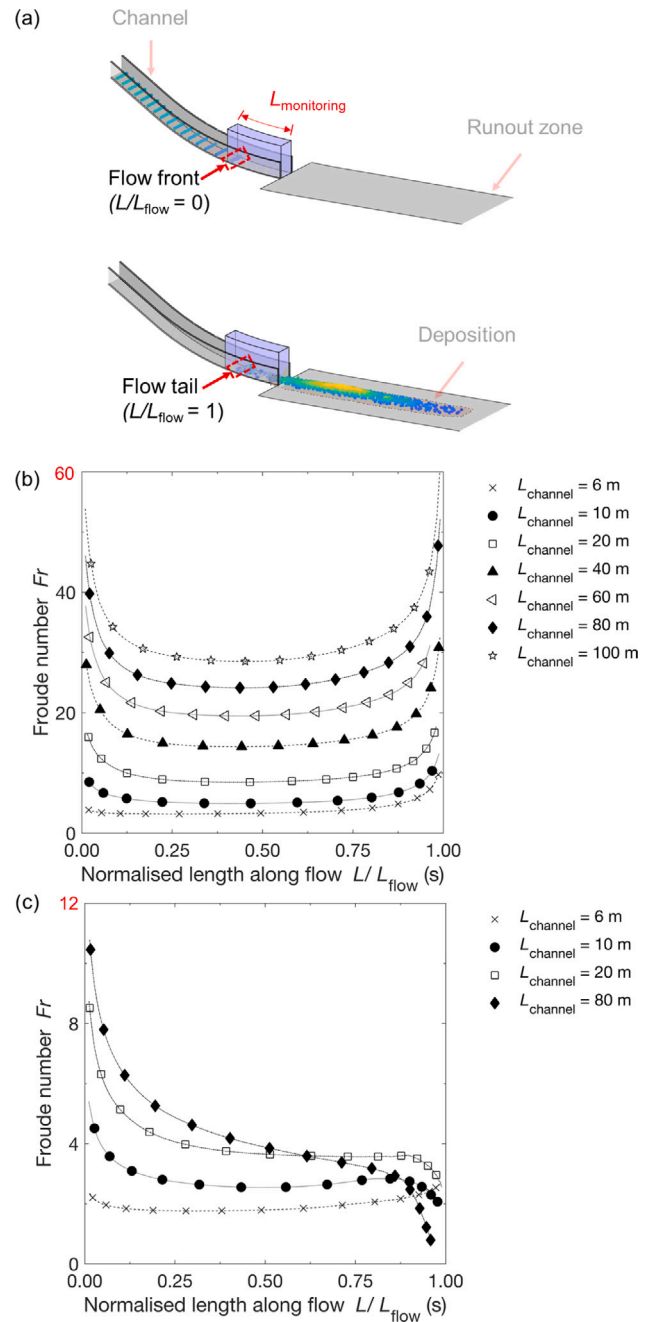


Fig. 14. Froude profiles along the length of various flows for volumes of 10 m^3 . Part (a) shows how the monitoring region is defined, i.e. the blue polygon. The front of the flow is defined as the first points entering the monitoring region. The tail of the flow is defined as the last points entering the monitoring region. Part (b) shows Froude profiles for water; and part (c) shows Froude profiles for debris.

Haas et al., 2018; Kang and Lee, 2018), the literature does not systematically link the spreading angle with the upstream flow conditions. The spreading angle was found by evaluating the position of each smoothed point relative to the edge of the mouth of the channel. Fig. 15a defines the monitoring section adopted. A cutoff point was set approximately 2 m away from the mouth of the channel to avoid spurious angles. Fig. 15b shows the angle of spreading for both liquid and debris flows exiting channels as a function of the maximum Froude number at the end of the channel. Fig. 15c shows the angle of spreading for just debris flows as a function of the flow volume.

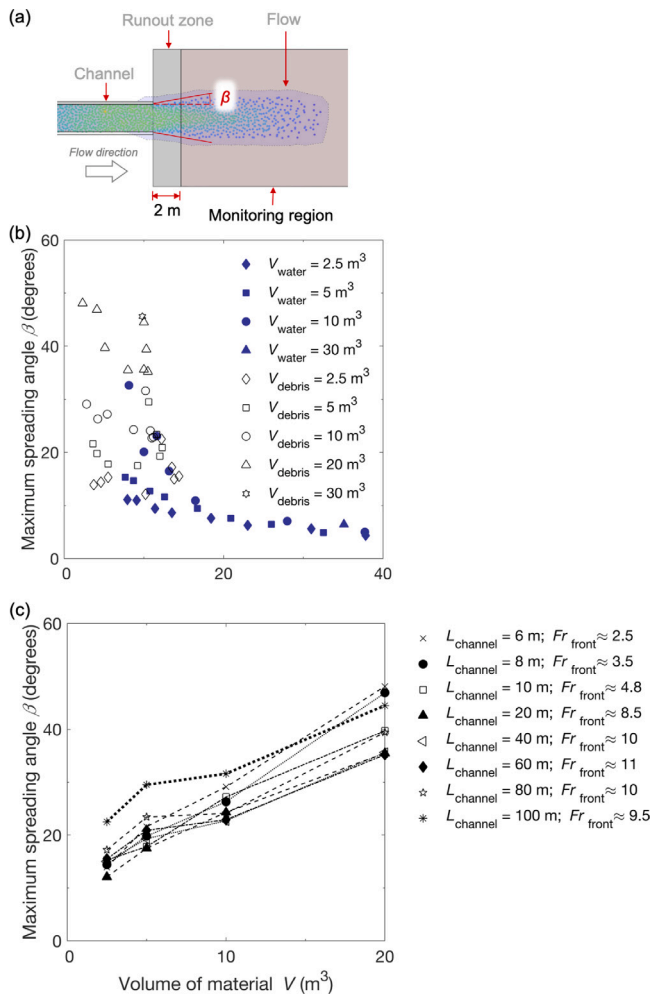


Fig. 15. Part (a) shows a plan view of the monitoring region, 2 m away from the mouth of the channel. Part (b) shows the spreading angle β for a variety of Fr and initial volumes; and part (c) shows the spreading angle β as a function of volume (for debris only).

Fig. 15b shows that the spreading angle for water is mostly a function of Fr_{front} , especially for highly supercritical flows. The scatter in the data is due to difficulties in sampling Fr_{front} over a wide variety of cases; this scatter largely disappears if Fr_{min} is adopted instead, although it is then difficult to characterise Fr for the debris flow cases (which often have no clearly-defined Fr_{min} ; see Fig. 14). This relationship with Fr is somewhat expected: water has a constant pressure coefficient k of unity, which indicates that it can spread equally in any direction at any point during the flow process. Since Fr compares the downstream velocity U with the root of the flow depth h , lower values of Fr would indicate that pressure gradients due to the flow depth would be relatively more important in driving spreading of the flow in all directions.

The spreading angles for debris flow material follow a different trend than water, and have little correlation with Fr . Instead, for debris, the spreading angle appears to be correlated with the volume of material rather than Fr , as shown in Fig. 15c. The main reason for the correlation with volume is because the flow material is able to pile up as it decelerates in the downstream debris basin. The shear strength of the decelerating debris thus causes the formation of an obstacle. This appears to be why higher volumes of material do not necessarily lead to much longer runout distances than flows with smaller volumes (Rickenmann, 2005); instead, incoming material is pushed aside by that which has already come to rest. More insight

into the mechanisms underpinning these different spreading angles are explored in the following section.

6.3. Deposit profiles

Fig. 16 shows the final deposition patterns for a range of Froude numbers Fr and initial volumes of material V . The two most obvious trends are (i) that increasing the volume of material enlarges the deposition area, both in the lateral and downstream directions; and (ii) that an increase in Fr tends to elongate the deposits, more so for smaller volumes of material.

A subtler phenomenon is the increase in channel length and hence Fr tending to cause flow material to become stuck in the channel. In contrast, for smaller Fr , the deposition is substantially further away from the channel mouth. In fact, the dependence on Fr is vital: lower Fr imply thicker flows, where a higher pressure gradient is available for driving the flow downstream. For the high Fr flows, passage of the flow in the runout zone is initially driven by the effects of the gravitational forces that were pulling the flow downslope. In contrast, for lower Fr flows, a substantial pressure gradient is still available for pushing the flow material out of the channel.

Furthermore, the four screenshots of Fr of around 4.8 show that flow material tends to pile up downstream directly in front of the mouth of the channel, forming an obstacle. The formation of this obstacle is enabled by the shear strength of the flow. The obstacle behaves rather like a column or a baffle (see for instance Tiberghien et al., 2007; Teufelsbauer et al., 2009; Choi et al., 2014; Faug, 2015b; Bi et al., 2018). Given an unlimited stream of oncoming material, the cheapest option energetically would be for flow material to be deflected to either side of the obstacle; this phenomenon is reflected by the increase in spreading angle reported earlier in the manuscript. The characteristics of this blockage change somewhat as Fr increases, tending to become narrower, rather than being shaped like a tear-drop. For initially higher Fr , oncoming flow material tends to be able to flow further downstream, rather than becoming part of a wider blockage, causing a somewhat higher proportion of material further downstream.

Damming of the channel due to the tail of a deposition could potentially be catastrophic, since the course of subsequent debris flows could be substantially altered. A hint of damming is seen even for the lowest Fr shown at the largest flow volume, implying that the volume of the flow is likely to be the governing factor for whether channels become blocked. This underscores the need for regular reconnaissance of vulnerable sites which have an ongoing history of large-volume flows.

6.4. Evolution of lateral earth pressure terms

At this stage, it is not obvious to what extent the lateral earth pressure forces or lateral earth pressure coefficient k_y influence the degree of lateral spreading for debris flows, relative to other factors (e.g. the basal resisting forces). To understand further the underlying mechanics of lateral spreading for flows of (i) water and (ii) debris, we sampled data from the corresponding tests simulating an 80-m channel. Lateral forces were sampled for each flow on both sides of the channel mouth; the force components on each side were then summed, and an average of the forces on both sides was then taken (accounting for sign differences). Each force component was determined using an equation of the following form:

$$F_y = \frac{1}{2} \left[\left(\sum_{q=1}^Q F_{y,q} \right)_{\text{left}} - \left(\sum_{q=1}^Q F_{y,q} \right)_{\text{right}} \right] \quad (46)$$

where 'left' and 'right' correspond to the two different sides of the channel.

Figs. 17a and 17b show the total lateral forces in this region as a function of time for water and debris respectively. Fig. 17c shows the

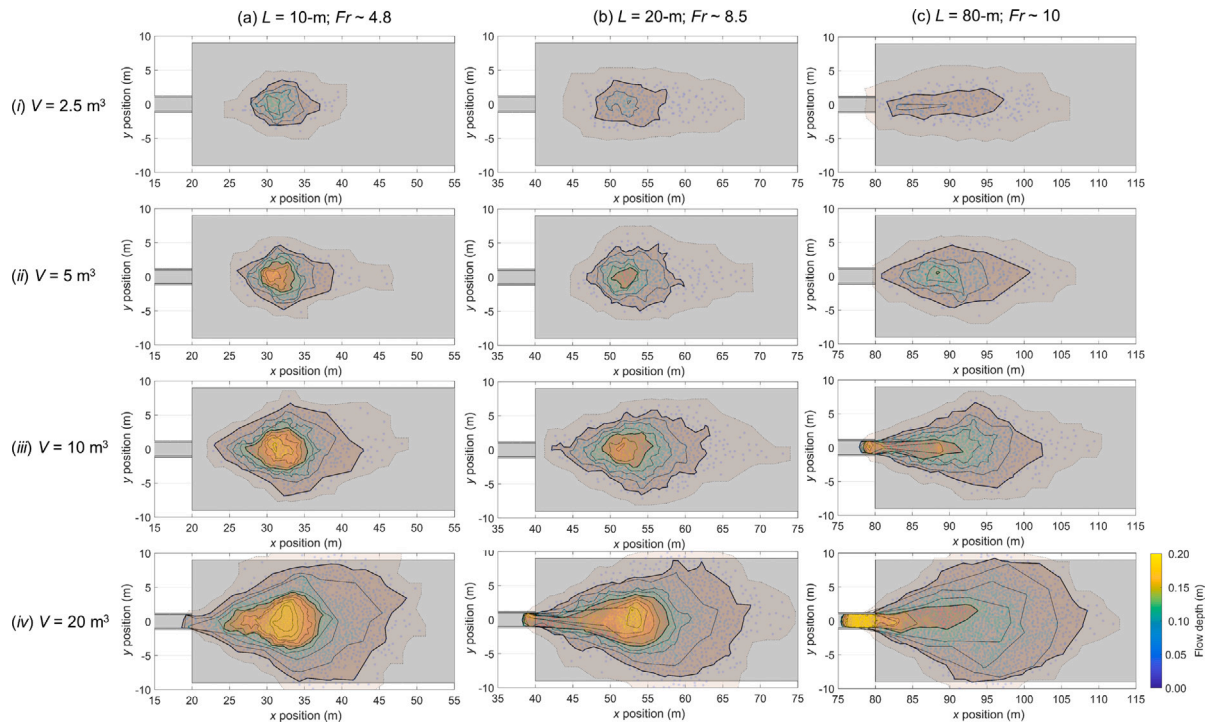


Fig. 16. Top-down views of the deposits for a range of flows, varying the channel length (and hence Fr) as well as the volume of flow material. The contour lines demarcate the flow at 0.02 m intervals.

evolution of the lateral earth pressure coefficient for the debris case along with the spreading angle. The two columns (i) and (ii) correspond to volumes of 10 and 30 m^3 respectively.

Figs. 17a(i) and 17a(ii) show that regardless of volume, the lateral pressure gradient is entirely responsible for driving lateral spreading of the flow. The influence of volume is simply to increase the forces driving lateral spreading, as reflected by the thicker flows and lower Fr , as already mentioned.

Fig. 17b shows the lateral forces for debris flows of different volumes. Fig. 17b(i) shows that forces due to the pressure gradient initially dominate the lateral behaviour of flows. Thereafter, Voellmy resisting forces (Hungr, 1995) start to oppose continued lateral spreading. Forces due to the basal friction ϕ_b grow continuously in magnitude as the direction of the flow shifts from downstream to cross-stream. Forces due to the Voellmy term ξ also increase, but only slightly due to the limited lateral velocity, and decreases again once the flow has started to come to rest. The total force stops driving lateral spreading at around $t = 1.7$ s after the flow has entered the monitoring section, and then starts to oppose spreading. Fig. 17b(ii) shows that the same general trend is apparent for the larger volume of material. As with the case of the Newtonian liquid, the magnitude of these lateral forces has increased with the volume. The main difference between the two volumes of material is that the lateral pressure gradient forces have increased substantially relative to the basal resisting forces. Although the total lateral forces stop promoting lateral spreading at around the same time as in the other case (i.e. at about $t = 1.7$ s, the transition is more gradual, with a clear drop occurring onto at $t = 2.3$ s. This delayed transition suggests that a larger volume of debris can be pushed to either side of the flow, and is related to the increased spreading angle for larger volumes.

To understand the effects of volume on the evolution of lateral spreading further, Fig. 17c shows both the lateral earth pressure coefficient k_y and the spreading angle. The instantaneous earth pressure is calculated as an average of all the points in the sampling region:

$$k_y = \frac{1}{Q} \sum_{q=1}^Q k_{y,q} \quad (47)$$

The upper and lower bounds of the earth pressure $k_{y\max}$ and $k_{y\min}$ are calculated in the same way using the individual instantaneous bounds for each of the smoothed points, which are a function of the prevailing downstream earth pressure, as defined in the Methodology (Eq. (33)) (see also McDougall and Hungr, 2004). The instantaneous maximum spreading angle β is obtained in the same way as in the data points in Fig. 15.

Fig. 17c(i) shows data for a volume $V = 10$ m^3 . At the point where monitoring starts, k_y is near $k_{y\min}$, since only points on either side of the mouth of the channel (i.e. those that have already undergone lateral spreading) are being sampled. The value of k_y increases to a maximum of nearly unity at about 0.5 s, and is relatively sustained at about $k_y = 0.7$ thereafter. This increase is due to the resisting forces due to the Voellmy terms ϕ_b and ξ in the downstream direction, which increase in magnitude as the flow moves further onto the debris basin and away from the channel. This downstream deceleration tends to cause the flow to thicken further, thus increasing the earth pressure terms in both the longitudinal and lateral directions. The sustained lateral earth pressure coefficient is correlated with a smoothly increasing total pressure gradient as more material enters the monitoring region.

The effects of volume on both k_y and β are evident by comparing Figs. 17c(i) ($V = 10$ m^3) and 17c(ii) ($V = 30$ m^3). In Fig. 17c(ii), k_y also increases initially due to the flow thickening under the influence of longitudinal deceleration. At around $t = 1$ s, k_y reaches its approximate final value of around 1.0, which is somewhat higher than in Fig. 17c(i). This higher value is indicative of a thicker deposit. The shear strength of the debris causes an obstacle to form, the depth of which is correlated with the volume of material; this in turn promotes a higher pressure gradient which tends to relax most easily in the lateral direction, since that is where the gradient tends to be highest. The net effect is for the obstacle to cause extra oncoming material to be pushed to the sides, which is why the spreading angle β is higher. It is worth noting that the total and pressure gradient forces are approximately the same for the case of water because the viscous resisting forces are negligible. In contrast, for the cases with debris flows, the basal friction and Voellmy ξ forces are large enough relative to the pressure gradient forces for the total force to be affected.

In summary, Figs. 15 and 17 highlight some of the fundamental differences between different material rheologies in terms of spreading behaviour. The spreading behaviour of Newtonian liquids is governed by Fr , whereas that of debris is governed by the volume of material. However, at this point it is not clear whether either phenomenon can facilitate a reduction in the impact loading on a hypothetical terminal barrier when compared with the so-called ‘free-field’ approach. This question is addressed in the following section.

6.5. Predicted impact forces on a barrier

In this section, we assess the predicted impact forces on a hypothetical barrier placed at various positions downstream. A schematic of some hypothetical barriers is shown in Fig. 18a.

Figs. 18b to 18d show the normalised calculated impact force per unit width on the ordinate and normalised downstream position on the abscissa. The per-width force is calculated using Eq. (3) (see Hübl et al., 2009; Kwan, 2012), adopting an α value of 1 for water and 1.5 for debris (Kwan and Koo, 2020). Within the SPH framework, the forces are calculated as follows, assuming that smoothed points have entered a particular monitoring region:

$$\left(\frac{F}{L}\right) = (h) (\alpha \rho U^2) \quad (48)$$

$$= \left(\sum_{q=1}^Q h_q\right) \left(\alpha \rho \sum_{q=1}^Q U_q^2\right) \quad (49)$$

The normalised impact force per unit width is that from a 3D simulation (i.e. allowing lateral spreading) vs. an equivalent 2D simulation (the ‘free-field’ approach, with no lateral spreading).

In Fig. 18b, each of the flows comprises water. Only one volume is shown ($V = 10 \text{ m}^3$), since it has already been established that the spreading behaviour of water is governed by Fr rather than volume (see Fig. 14). It should be noted that although the Fr_{front} values quoted are rather high, the values in the middle of the flow (which are more representative for longer flows) are typically about half the value of Fr_{front} (see Fig. 14). Each of the data series shows that further down the debris basin, the impact force per unit width reduces relative to the free-field approach, as expected. The reduction in the calculated impact force is greatest for the flow with the lowest Fr_{front} . This is because the spreading angle is highest for this case (Fig. 15), and the effect of the flow running out so far is enough to cause it to become shallow enough to reduce the potential impact force greatly. There is a reduction in the impact force for the lowest Fr of around 70% that of the equivalent load for a 2D flow at a distance of 20 m downstream. For $Fr_{\text{front}} = 27.9$, the reduction is around 50% at 20 m from the channel mouth, which is still very substantial. The results from Fig. 18b show that even for short basins, substantial reductions in the impact force requirements for terminal barriers can be achieved for flows governed by viscous stresses, as compared with 2D analyses that do not consider lateral spreading.

Fig. 18c shows calculated impact forces for 10 m^3 of debris flow material. Within the first 5 m, the calculated impact forces for the 2D and 3D cases are the most similar, although the 3D analysis gives a reduction in impact for of between 10 and 50%. In this region, the peak calculated force for the 3D case occurs when the flow momentum is mostly oriented downstream. Further than 5 m downstream, lateral spreading for flows in the 3D analyses has reduced the volume of flow material flowing downstream, and hence the flow depth. Thus, the calculated impact force from the 3D cases is generally lower than the 2D cases. Moreover, the non-normalised calculated impact force for this region in the 3D analysis is minimal in any case (as shown in the smaller right-hand figure), indicating that most of the flow material has already come to rest further upstream. (It should be noted that the increase in normalised impact force for the three highest Froude numbers more than about 10 m downstream is inconsequential. This

is because the forces at this point downstream are already very low, compared to near the outlet.)

Fig. 18d shows that doubling the volume of debris ($V = 20 \text{ m}^3$) tends to lead to a further reduction in the normalised calculated force, compared to Fig. 18c. This is because the extra volume of material does not tend to increase the runout length (Rickenmann, 2005). Instead, the shear strength of the debris material causes the formation of an obstacle that is mound-shaped for low Fr and progressively more elongated as Fr increases. The mound tends to cause further oncoming material to be shunted aside laterally (see Fig. 13). Since this mechanism is not available in 2D ‘free-field’ approaches, the ‘free-field’ approach becomes very conservative relative to the 3D one. Indeed, for the case considered in 18d, if a barrier was intended to be placed 10 m downstream from a channel, adopting a 3D approach could lead to a reduction in the required impact force per unit width of between 50 and 75%.

It can also be noted an obstacle can be formed by depositing debris, although it is somewhat dependent on the longitudinal profile of the upstream Froude number. These obstacles are consistent with those observed in the USGS video repository (Logan et al., 2018), but distinct from the ‘mobile dam’ mechanism described in (Jakob and Hungr, 2005). The obstacle – which is mound-shaped for low Fr and progressively more elongated as Fr increases (see Fig. 16) – occurs in both 2D and 3D cases. However, there is a route for the flow material around the obstacle only in the 3D case, which is why there is a rise in the calculated force for the 3D case but not the 2D case – at least for low Fr . Indeed, this effect is not observed at high Fr because the channel is effectively dammed by the flow material (see Fig. 16), preventing upstream flow material from continuing to flow downstream. Nonetheless, for the low Fr cases, the difference in calculated impact forces is rather small as of 5 to 10 m downstream from the channel mouth, as evidenced by the right-hand side plots of the actual calculated forces. The competing effects caused by the mounds and the ability of the flow to spread are thus relatively minor.

A few final comments are warranted. Firstly, it should be acknowledged that the force calculation method, whilst adopted in industry (e.g. Kwan, 2012), is only an approximation (Song et al., 2019), especially if many large hard inclusions are anticipated. Secondly, it is worth emphasising that if lateral levees are anticipated, which have the effect of inhibiting lateral spreading (e.g. Iverson et al., 2010; George and Iverson, 2014), the free-field (2D) approach may give more reasonable results. Furthermore, the critical distances identified in this section are around 10 m, for the 3D approach to give lower per-unit run values of impact force compared to the free-field (2D) approach. To give some idea of the potential reductions in design force that could be realised, Cosenza et al. (2006) indicates that the debris basin shown in Fig. 1a has a retention capacity of $22,000 \text{ m}^3$, although the authors do not give the exact dimensions of the debris basin. If shaped as a cube, $22,000 \text{ m}^3$ of debris would have sides of 28 m; the basin is triangular in shape, and debris seems unlikely to pile up to a height of 28 m, so the actual length of the basin is probably much longer. Of course, for such enormous volumes, the runout distance would likely be longer than the flows in this study. Nonetheless, this study highlights that detailed 3D studies of the dynamics of flows entering basins may well allow engineers to avoid needlessly over-conservative values for the design force on terminal barriers.

Furthermore, determining a scaling relationship between the various variables (Fr , flow volume V , channel width B etc.) should be the end goal of the present line of research. However, as the results from this manuscript show, the relationships between Fr , V and the impact force and deposition profiles are highly non-linear. This non-linearity is due to many interacting factors, even within our highly simplified model, including (for instance) the forces due to the pressure gradient available for driving the flow downstream as the flow reaches the runout zone. Consequently, it seems that there is no obvious variable for non-dimensionalising the results pertaining to impact force. A much

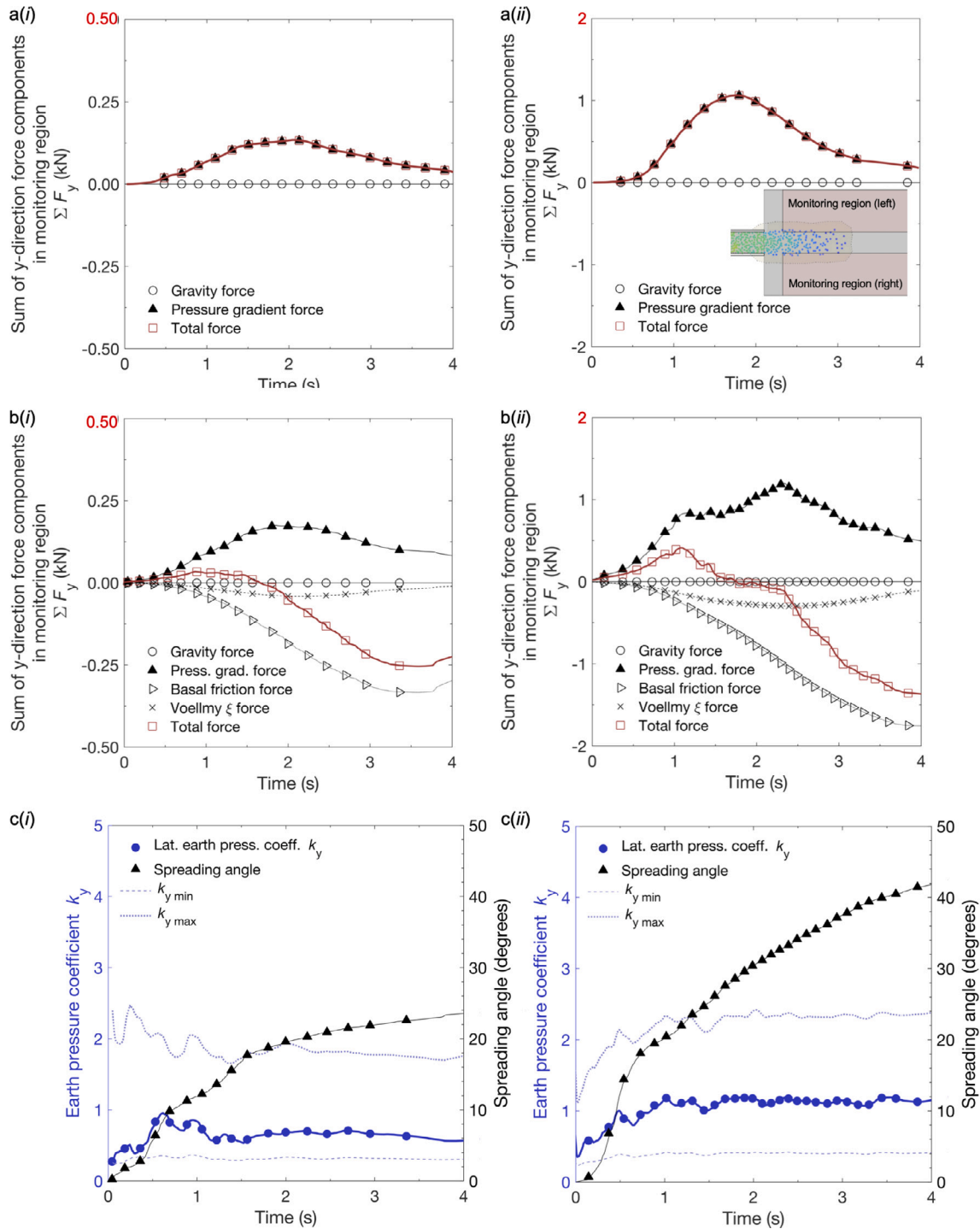


Fig. 17. Evolution of the lateral force components for (a) a water flow and (b) a debris flow. The inset in (a) shows the position of the monitoring regions. Part (c) shows the evolution of the lateral earth pressure coefficient k_y with the spreading angle. The instantaneous lateral earth pressure bounds are also shown. Column (i) corresponds to a volume V of 10 m^3 whilst column (ii) is a volume V of 30 m^3 .

broader parametric study would be required to isolate the relevant combinations of variables, and the ranges over which they govern the downstream flow behaviour; this would be a valuable topic for future research.

7. Conclusions

In this study, a depth-averaged SPH model coded specifically for the purpose of understanding spreading mechanisms was developed. Physical dam-break tests using (i) water and (ii) dry sand running out

onto an unconfined planar surface were performed to evaluate fluid and frictional Voellmy rheological models implemented in the depth-averaged SPH program. Established analytic models also validated the implementation. A large-scale test from Iverson et al. (2010) was also adopted for evaluation of the model.

The SPH model was used for a parametric study on material type, material volume, upstream channel length (and hence the Froude number Fr) and the lateral confinement. The aim was to evaluate potential improvements to the 2D ‘free field’ approach used for current barrier design by comparing it with 3D analyses, which allow consideration

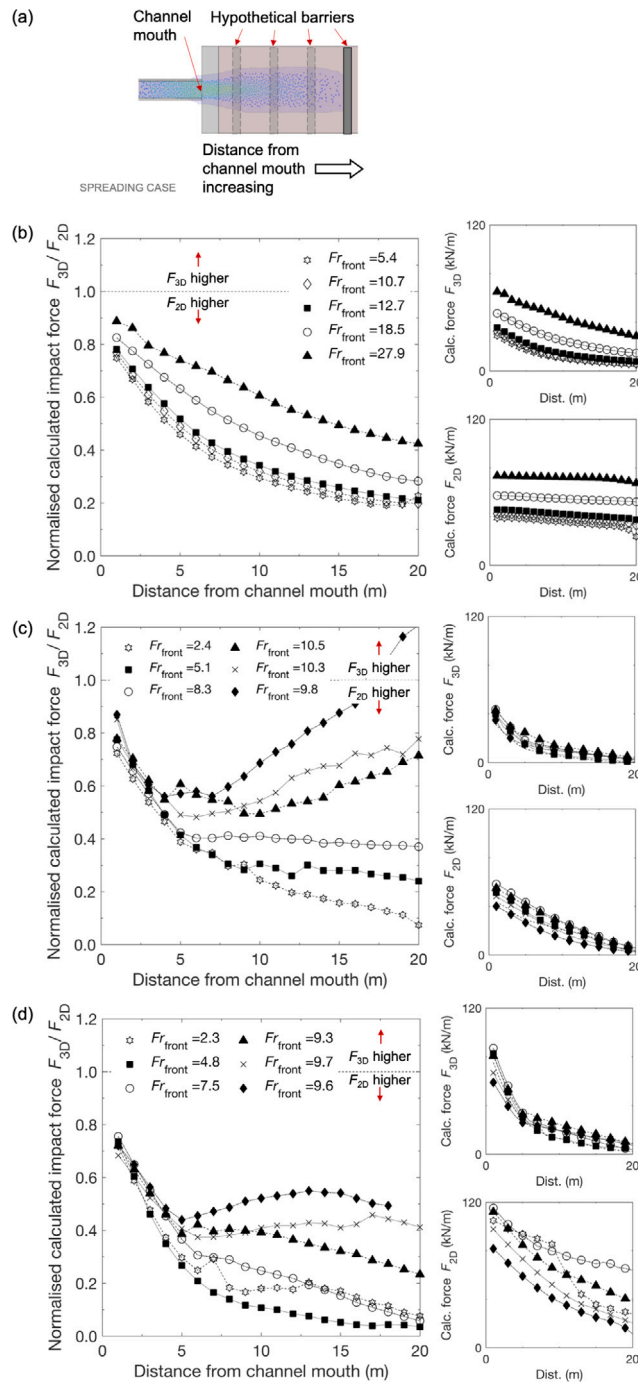


Fig. 18. Part (a) shows the measuring region and hypothetical barriers adopted for the 3D cases (where lateral spreading is being modelled). Parts (b) to (d) show the reduction in the computed force on a barrier at different distances downstream for different flow types: (b) is water, and (c) and (d) are debris. The volumes of material for each case are (b) 10 m^3 , (c) 10 m^3 , and (d) 20 m^3 . The Fr in the legends indicate maximum values within the channel, near the mouth. The forces for each line represent those calculated from simulations where spreading was allowed, vs. those where it was not (i.e. the so-called ‘freefield’ condition, which treats flows as though they are 2D.) The smaller side graphs show non-normalised force for the 3D and 2D cases (where lateral spreading was and was not allowed, respectively).

of lateral flow spreading. The ‘free field’ approach neglects lateral spreading, and the effects thereof on flow depth and velocity.

Key findings from this study are as follows:

1. For water, the spreading angle is correlated with Fr , since it has no internal strength and tends to flow under the influence of gravity. In contrast, for debris, lateral spreading is governed by the volume of material, with larger volumes leading to greater degrees of spreading. This is due to the internal strength of debris which tends to allow such flows to pile up and form an

obstacle, which is mound-shaped for low Fr and progressively more elongated as Fr increases. As such, the preferential path for further oncoming debris is around the deposits, thus causing lateral spreading. Furthermore, the degree of spreading for debris is governed by multiple inter-related processes, including longitudinal basal resisting forces which cause the flow to decelerate, as well as the lateral earth pressure coefficient. Lateral resisting forces limit the degree of spreading possible.

2. For both frictional and viscous flow types, the impact force requirements for terminal barriers could be reduced by more

than 50% when compared to continuously channelised flows (i.e. flows modelled under the assumption of 2D free-field conditions). Nonetheless, frictional flows containing a range of grain sizes, and which are thus likely to cause lateral levee formation downstream, would better be dealt with using 2D analyses. These 2D analyses implicitly account for the continued downstream confining effects due to these levees. Furthermore, it is necessary for barriers to be placed a certain distance downstream from the channel mouth (5 m+ for the channels, basins and volumes of flow material modelled in this study) to fully take advantage of arrested debris flow material causing other oncoming flow material to fan out.

- Collectively, these findings imply that the volume of debris flows constitutes an important source of scale effects for flow spreading, with larger volumes not necessarily being substantially more dangerous within a certain range (about an order of magnitude in this study). Indeed, a comparison of quasi-2D and quasi-3D approaches show that an increase in volume of the flow material makes the 2D approach proportionately more conservative. This is ultimately because of the increase in spreading angle for larger volumes of flow, which would tend to spread out the load across the width of a hypothetical barrier. As a consequence, debris flow basins and terminal barriers may be more resilient to uncertainty in the volume of material than may typically be assumed. It is nonetheless worth noting 2D approaches seem to indirectly account for features such as lateral levee formation by not allowing lateral spreading. The likely composition of a flow must thus be accounted for when determining whether a 2D or 3D analysis is more appropriate for a given case. Detailed 3D studies of the dynamics of flows entering basins may well allow engineers to avoid needlessly over-conservative values for the design force on terminal barriers.

CRedit authorship contribution statement

George Robert Goodwin: Drafting, Writing - review & editing, Interpretation of data, Coding the numerical model, Writing - original draft. **Clarence Edward Choi:** Drafting, Writing - review & editing, Interpretation of data, Developing the idea of investigating lateral flow spreading.

Declaration of competing interest

The authors declare that they have no known competing financial interests or personal relationships that could have appeared to influence the work reported in this paper.

Acknowledgements

The authors are thankful for the funding from the Research Grants Council of Hong Kong (General Research Fund Grants 16212618 and 16210219), the Early Career Scheme grant 72205320, and the Area of Excellence GRANT AoE/E-603/18. Furthermore, some of the work was performed whilst the first author was working in France under funding graciously provided as part of the MOPGA 2021–22 scheme (MOPGA-976501H), from the Agence Nationale de la Recherche (France). Funding was also provided by the INTPART project “Landslide mitigation of Urbanized slopes for sustainable growth” funded by the Research Council of Norway.

References

- Abe, K., Konagai, K., 2016. Numerical simulation for runout process of debris flow using depth-averaged material point method. *Soils Found.* 56, 869–888.
- Albaba, A., Lambert, S., Faug, T., 2018. Dry granular avalanche force on a rigid wall: analytic shock solution versus discrete element simulations. *Phys. Rev. E* 97, 052903.
- Ancey, C., Cochard, S., 2009. The dam-break problem for Herschel-Bulkley viscoplastic fluids down steep flumes. *J. Non-Newton. Fluid Mech.* 158 (1–3), 18–35. <http://dx.doi.org/10.1016/j.jnnfm.2008.08.008>.
- Armanini, A., 2015. Closure relations for mobile bed debris flows in a wide range of slopes and concentrations. *Adv. Water Resour.* 81, 75–83.
- Armanini, A., Larcher, M., Nucci, E., Dumbser, M., 2014. Submerged granular channel flows driven by gravity. *Adv. Water Resour.* 63, 1–10.
- Armanini, A., Larcher, M., Odorizzi, M., 2011. Dynamic impact of debris flow front against a vertical wall. In: Proceedings of the 5th International Conference on Debris-Flow Hazards Mitigation: Mechanics, Prediction and Assessment 2011, pp. 1041–1049.
- Ashwood, W., Hungri, O., 2016. Estimating total resisting force in flexible barrier impacted by a granular avalanche using physical and numerical modelling. *Can. Geotech. J.* 81 (10), 1700–1717.
- Berti, M., Simoni, A., 2007. Prediction of debris flow inundation areas using empirical mobility relationships. *Geomorphology* 90, 144–161. <http://dx.doi.org/10.1016/j.geomorph.2007.01.014>.
- Bi, Y., Du, Y., He, S., Sun, X., Wang, D., Li, X., Liang, H., Wu, Y., 2018. Numerical analysis of effect of baffle configuration on impact force exerted from rock avalanche. *Landslides* 15, 1029–1043.
- Bui, H.H., Fukagawa, R., Sako, K., Ohno, S., 2008. Lagrangian meshfree particles method (SPH) for large deformation and failure flows of geomaterial using elastic-plastic soil constitutive model. *Int. J. Numer. Anal. Methods Geomech.* 32 (12), 1537–1570. <http://dx.doi.org/10.1002/nag.688>.
- Canelli, L., Ferrero, A., Migliazza, M., Segalini, A., 2012. Debris flow risk mitigation by the means of rigid and flexible barriers—experimental tests and impact analysis. *Nat. Hazards Earth Syst. Sci.* 12 (5), 1693–1699.
- Chalk, C., Pastor, M., Borman, D., Sleight, A., Peakall, J., Murphy, W., Fuentes, R., 2017. A smoothed particle hydrodynamics study of an experimental debris flow. In: Proceedings of the 4th World Landslide Forum 2017. Springer, pp. 573–578.
- Chambon, G., Bouvarel, R., Laigle, D., Naaim, M., 2011. Numerical simulations of granular free-surface flows using smoothed particle hydrodynamics. *J. Non-Newton. Fluid Mech.* 166 (12), 698–712. <http://dx.doi.org/10.1016/j.jnnfm.2011.03.007>.
- Chengara, A., Nikolov, A.D., Wasan, D.T., 2007. Spreading of a water drop triggered by the surface tension gradient created by the localized addition of a surfactant. *Ind. Eng. Chem. Res.* 46 (10), 2987–2995. <http://dx.doi.org/10.1021/ie060695y>.
- Cheuk, C.Y., White, D.J., Bolton, M.J., 2008. Uplift mechanisms of pipes buried in sand. *J. Geotech. Geoenviron. Eng. (ASCE)* 134 (2), 154–163.
- Choi, C.E., Au-Yeung, S.C.H., Ng, C.W.W., Song, D., 2015a. Flume investigation of landslide granular debris and water runup mechanisms. *Geotech. Lett.* 5, 28–32.
- Choi, C.E., Goodwin, G.R., 2021. Effects of interactions between transient granular flows and macroscopically rough beds and their implications for bulk flow dynamics. *Can. Geotech. J.* <http://dx.doi.org/10.1139/cgj-2020-0160>.
- Choi, C.E., Ng, C.W.W., Au-Yeung, S.C.H., Goodwin, G.R., 2015b. Froude characteristics of dense granular and water flows in flume modelling. *Landslides* 12 (6), 1197–1206.
- Choi, C.E., Ng, C.W.W., Law, R.P.H., Song, D., Kwan, J.S.H., Ho, K.K.S., 2015c. Computational investigation of baffle configuration on impedance of channelized debris flow. *Can. Geotech. J.* 52 (2), 182–197.
- Choi, C.E., Ng, C.W.W., Song, D., Kwan, J.S.H., Shiu, H.Y.K., Ho, K.K.S., Koo, R.C.H., 2014. Flume investigation of landslide debris-resisting baffles. *Can. Geotech. J.* 51 (5), 540–553.
- Cosenza, E., Cozzolino, L., Pianese, D., Fabbrocino, G., Acanfora, M., 2006. Concrete structures for mitigation of debris-flow hazard in the Montoro Inferiore Area, Southern Italy. In: 2nd International Congress, IFSC, pp. 1–12.
- Crespo, A.J.C., Domínguez, J.M., Rogers, B.D., Gómez-Gesteira, M., Longshaw, S., Canelas, R., Vacondio, R., Barreiro, A., García-Feal, O., 2015. DualSPHysics: Open-source parallel CFD solver based on smoothed particle hydrodynamics (SPH). *Comput. Phys. Comm.* 187, 204–216. <http://dx.doi.org/10.1016/j.cpc.2014.10.004>.
- Cundall, P.A., Strack, O.D.L., 1979. A discrete numerical model for granular assemblies. *Géotechnique* 29 (1), 47–65.
- de Haas, T., Densmore, A.L., Stoffel, M., Suwa, H., Imaizumi, F., Ballesteros-Cánovas, J.A., Waskiewicz, T., 2018. Avulsions and the spatio-temporal evolution of debris-flow fans. *Earth-Sci. Rev.* 177, 53–75. <http://dx.doi.org/10.1016/j.earscirev.2017.11.007>.
- de Linares, M.G., Mano, V., Piton, G., Recking, A., 2020. Modelling of massive bedload deposition in a debris basin: cross comparison between numerical and small scale modelling. In: *River Flow 2020: Proceedings of the 10th Conference on Fluvial Hydraulics*. Praxis Springer, pp. 282–289.
- Faug, T., 2015a. Depth-averaged solutions for free-surface granular flows impacting rigid walls down inclines. *Phys. Rev. E* 92, 062310.
- Faug, T., 2015b. Macroscopic force experienced by extended objects in granular flows over a very broad froude-number range. *Eur. Phys. J. E* 38 (34), 1–10.

- Faug, T., 2020. Impact force of granular flows on walls normal to the bottom: slow versus fast impact dynamics. *Can. Geotech. J.* 58, 114–124. <http://dx.doi.org/10.1139/cgj-2019-0399>.
- Faug, T., Beguin, R., Chanut, B., 2009. Mean steady granular force on a wall overflowed by free-surface gravity-driven dense flows. *Phys. Rev. E* 80, 021305. <http://dx.doi.org/10.1103/PhysRevE.80.021305>.
- Faug, T., Naaim, M., Bertrand, D., Lachamp, P., 2003. Varying dam height to shorten the run-out of dense avalanche flows: developing a scaling law from laboratory experiments. *Surv. Geophys.* 24 (5–6), 555–568.
- Favier, L., Daudon, D., Donzé, F.-V., Mazars, J., 2009. Predicting the drag coefficient of a granular flow using the discrete element method. *J. Stat. Mech. Theory Exp.* 9, P06012. <http://dx.doi.org/10.1088/1742-5468/2009/06/P06012>.
- FHA (Federal Highway Administration), 2006. Hydraulic design of energy dissipators for culverts and channels, Hydraulic Engineering Circular No. 14, Publication No. FHWA-NHI-06-086, third ed. US Department of Transportation.
- Froude, M.J., Petley, D.N., 2018. Global fatal landslide occurrence from 2004 to 2016. *Nat. Hazards Earth Syst. Sci.* 18, 2161–2181. <http://dx.doi.org/10.5194/nhess-18-2161-2018>.
- GEO, 2008. Study on the landscape treatment for debris-resisting barriers. GEO Report No. 256, Geotechnical Engineering Office, Civil Engineering and Development Department, The HKSAR Government.
- George, D.L., Iverson, R.M., 2014. A depth-averaged debris-flow model that includes the effects of evolving dilatancy. II. Numerical predictions and experimental tests. *Proc. R. Soc. A Math. Phys. Eng. Sci.* 470, 20130820. <http://dx.doi.org/10.1098/rspa.2013.0820>.
- Goodwin, G.R., Choi, C.E., 2020. Slit structures: Fundamental mechanisms of mechanical trapping of granular flows. *Comput. Geotech.* 119, 103376. <http://dx.doi.org/10.1016/j.compgeo.2019.103376>.
- Goodwin, G.R., Choi, C.E., Yune, C.-Y., 2021. Towards rational use of baffle arrays on sloped and horizontal terrain for filtering boulders. *Can. Geotech. J.* <http://dx.doi.org/10.1139/cgj-2020-0363>.
- Gray, J.M.N.T., Tai, Y.C., Noelle, S., 2003. Shock waves, dead-zones and particle-free regions in rapid granular free-surface flows. *J. Fluid Mech.* 491, 161–181.
- Gray, J.M.N.T., Wieland, M., Hutter, K., 1999. Gravity driven free surface flow of granular avalanches over complex basal topography. *Proc. R. Soc. Lond. Ser. A* 455, 1841–1874.
- Hübl, J., Suda, J., Proske, D., 2009. Debris flow impact estimation steep slopes. In: *Proceedings of the 11th International Symposium on Water Management and Hydraulic Engineering*, pp. 1–5.
- Huggel, C., Kääb, A., Haeblerli, W., Krummenacher, B., 2003. Regional-scale GIS-models for assessment of hazards from glacier lake outbursts: evaluation and application in the Swiss Alps. *Nat. Hazards Earth Syst. Sci.* 3 (6), 647–662. <http://dx.doi.org/10.5194/nhess-3-647-2003>.
- Hungr, O., 1995. A model for the runout analysis of rapid flow slides, debris flows and avalanches. *Can. Geotech. J.* 32, 610–623.
- Hungr, O., 2008. Simplified models of spreading flow of dry granular material. *Can. Geotech. J.* 45, 1156–1168. <http://dx.doi.org/10.1139/T08-059>.
- Iaconeta, I., Larese, A., Rossi, R., Oñate, E., 2017. An implicit material point method applied to granular flows. *Procedia Eng.* 175, 226–232. <http://dx.doi.org/10.1016/j.proeng.2017.01.017>.
- Iverson, R.M., 1997. The physics of debris flows. *Rev. Geophys.* 35 (3), 245–296. <http://dx.doi.org/10.1029/97RG00426>.
- Iverson, R.M., 2003. The debris-flow rheology myth. In: *Debris-Flow Hazards Mitigation: Mechanics, Prediction and Assessment*. Mill Press, pp. 303–314.
- Iverson, R.M., 2005. Regulation of landslide motion by dilatancy and pore pressure feedback. *J. Geophys. Res.: Earth Surface* 110 (F2), 1–16. <http://dx.doi.org/10.1029/2004JF000268>.
- Iverson, R.M., George, D.L., 2014. A depth-averaged debris-flow model that includes the effects of evolving dilatancy. I. Physical basis. *Proc. R. Soc. A: Math. Phys. Eng. Sci.* 470, 20130819. <http://dx.doi.org/10.1098/rspa.2013.0819>.
- Iverson, R.M., George, D.L., 2019. Valid debris-flow models must avoid hot starts. In: *Proceedings of the 7th International Conference on Debris-Flow Hazards Mitigation. Association of Environmental and Engineering Geologists (AEG)*, pp. 25–32.
- Iverson, R.M., George, D.L., Logan, M., 2016. Debris flow runup on vertical barriers and adverse slopes. *J. Geophys. Res.: Earth Surf.* 121, 2333–2357. <http://dx.doi.org/10.1002/2016JF003933>.
- Iverson, R.M., Logan, M., LaHusen, R., Berti, M., 2010. The perfect debris flow? Aggregated results from 28 large-scale experiments. *J. Geophys. Res.: Earth Sci.* 115, F03005. <http://dx.doi.org/10.1029/2009JF001514>.
- Iverson, R.M., Schilling, S.P., Vallance, J.W., 1998. Objective delineation of lahar-inundation hazard zones. *Geol. Soc. Am. Bull.* 110, 972–984.
- Jakob, M., Hungr, O., 2005. *Debris-Flow Hazards and Related Phenomena*. Praxis Springer.
- Jiang, Y., Towhata, I., 2013. Experimental study of dry granular flow and impact behavior against a rigid retaining wall. *Rock Mech. Rock Eng.* 46 (4), 713–729.
- Jing, L., Kwok, C.Y., Leung, Y.F., Leung, Y.F., Zhang, Z., Dai, L., 2018. Runout scaling and deposit morphology of rapid mudflows. *J. Geophys. Res.: Earth Surf.* 123, 2004–2023. <http://dx.doi.org/10.1029/2018JF004667>.
- Johnson, P.A., McCuen, R.H., Hromadka, T.V., 1991. Debris basin policy and design. *J. Hydrol.* 123 (1–2), 83–95. [http://dx.doi.org/10.1016/0022-1694\(91\)90070-X](http://dx.doi.org/10.1016/0022-1694(91)90070-X).
- Jonsson, P., Andreasson, P., Gunnar, J., Hellström, I., Jönsén, P., Lundström, T.S., 2016. Smoothed particle hydrodynamic simulation of hydraulic jump using periodic open boundaries. *Appl. Math. Model.* 40, 8391–8405.
- Kafle, J., Kattel, P., Mergili, M., Fischer, J.-T., Pudasaini, S., 2019. Dynamic response of submarine obstacles to two-phase landslide and tsunami impact on reservoirs. *Acta Mech.* 230, 3143–3169.
- Kang, S., Lee, S.-R., 2018. Debris flow susceptibility assessment based on an empirical approach in the central region of South Korea. *Geomorphology* 308, 1–12. <http://dx.doi.org/10.1016/j.geomorph.2018.01.025>.
- Kattel, P., Kafle, J., Fischer, J.-T., Mergili, M., Tuladhar, B., Pudasaini, S.P., 2018. Interaction of two-phase debris flow with obstacles. *Eng. Geol.* 242, 197–217.
- Kessler, M., Heller, V., Turnbull, B., 2020. Grain Reynolds number scale effects in dry granular slides. *J. Geophys. Res.: Earth Surf. (AGU)* 125, <http://dx.doi.org/10.1029/2019JF005347>.
- Kwan, J.S.H., 2012. Supplementary technical guidance on design of rigid debris-resisting barriers. Technical Note No. TN 2/2012, Geotechnical Engineering Office, Civil Engineering and Development Department, The HKSAR Government.
- Kwan, J.S.H., Koo, R.C.H., 2020. Enhanced technical guidelines for design of debris-resisting barriers. GEO Report No. 333, Geotechnical Engineering Office, Civil Engineering and Development Department, The HKSAR Government.
- Kwan, J.S.H., Koo, R.C.H., Lam, C., 2016. Updates of design guidance of rigid debris-resisting barriers. Technical Guidance Note No. 47 (TGN 47), Geotechnical Engineering Office, Civil Engineering and Development Department, The HKSAR Government.
- Kwan, J.S.H., Sun, H.W., 2006. An improved landslide mobility model. *Can. Geotech. J.* 43, 531–539.
- Kwan, J.S.H., Sun, H.W., 2007. Benchmarking exercise on landslide mobility modelling - runout analyses using 3ddmm. In: *Proceedings of the 2007 International Forum on Landslide Disaster Management*. Hong Kong Institute of Engineers (HKIE), pp. 945–966.
- Laigle, D., Lachamp, P., Naaim, M., 2007. SPH-based numerical investigation of mudflow and other complex fluid flow interactions with structures. *Comput. Geosci.* 11 (4), 297–306.
- Law, R.P.H., Choi, C.E., Ng, C.W.W., 2015. Discrete element investigation of the influence of granular debris flow baffles on rigid barrier impact. *Can. Geotech. J.* 53 (2), 179–185.
- Leonardi, A., Goodwin, G.R., Pirulli, M., 2019. The force exerted by granular flows on slit dams. *Acta Geotech.* 14, 1949–1963.
- Leonardi, A., Wittel, F.K., Mendoza, M., Vetter, R., Herrmann, H.J., 2016. Particle-structure interaction for debris flow impact on flexible barriers. *Comput.-Aided Civ. Infrastruct. Eng.* 31 (5), 323–333.
- Liu, G.-R., Liu, M.B., 2003. *Smoothed Particle Hydrodynamics: A Meshfree Particle Method*. World Scientific Publishing Co Pte Ltd.
- Logan, M., Iverson, R.M., Obryk, M.K., 2018. Video documentation of experiments at the USGS debris-flow flume 1992–2017 (ver 1.4, January 2018). U.S. Geological Survey Open-File Report 2007–1315, U. S. Geological Survey, Reston, VA, <http://dx.doi.org/10.3133/ofr20071315>.
- Mancarella, D., Hungr, O., 2010. Analysis of runup of granular avalanches against steep, adverse slopes and protective barriers. *Can. Geotech. J.* 47 (8), 827–841.
- Mangeny, A., Heinrich, P., Roche, R., 2000. Analytical solution for testing debris avalanche numerical models. *Pure Appl. Geophys.* 157 (6–8), 1081–1096.
- Martinez, C.E., 2009. Eulerian-Lagrangian two-phase debris flow model. (Ph.D. thesis). Florida International University.
- McDougal, S., Hungr, O., 2004. A model for the analysis of rapid landslide motion across three-dimensional terrain. *Can. Geotech. J.* 41, 1084–1097. <http://dx.doi.org/10.1139/T04-052>.
- Micheline, T., Bettella, F., D'Agostino, V., 2017. Field investigations of the interaction between debris flows and forest vegetation in two alpine fans. *Geomorphology* 279, 150–164. <http://dx.doi.org/10.1016/j.geomorph.2016.09.029>.
- Moriguchi, S., Borja, R.I., Yashima, A., Sawada, K., 2009. Estimating the impact force generated by granular flow on a rigid obstruction. *Acta Geotech.* 4, 57–71.
- Müller, M., Charypar, D., Gross, M., 2003. Particle-based fluid simulation for interactive applications. In: *Eurographics/SIGGRAPH Symposium on Computer Animation (2003)*. pp. 1–7.
- Ng, C.W.W., Choi, C.E., Goodwin, G.R., 2019. Froude characterisation for unsteady single-surge dry granular flows: impact pressure and runup height. *Can. Geotech. J.* 56 (12), 1968–1978. <http://dx.doi.org/10.1139/cgj-2018-0529>.
- Ng, C.W.W., Choi, C.E., Law, R.P.H., 2013. Longitudinal spreading of granular flow in trapezoidal channels. *Geomorphology* 194, 84–93. <http://dx.doi.org/10.1016/j.geomorph.2013.04.016>.
- Ng, C.W.W., Choi, C.E., Liu, L.H.D., Wang, Y., Song, D., Yang, N., 2017. Influence of particle size on the mechanism of dry granular run-up on a rigid barrier. *Geotech. Lett.* 7 (1), 79–89. <http://dx.doi.org/10.1680/jgele.16.00159>.
- Ng, C.W.W., Song, D., Choi, C.E., Liu, L.H.D., Kwan, J.S.H., Koo, R.C.H., Pun, W.K., 2016. Flexible mechanisms of granular and viscous flows on rigid and flexible barriers. *Can. Geotech. J.* 54 (2), 188–206.
- Ni, X., Sheng, J., Feng, W., 2016. Simulation of free-surface flow using the smoothed particle hydrodynamics (SPH) method with radiation open boundary conditions. *J. Atmos. Ocean. Technol.* 33, 2435–2460. <http://dx.doi.org/10.1175/JTECH-D-15-0179.1>.

- Park, D.W., Lee, S.R., Vasu, N.N., Kang, S.H., Park, J.Y., 2016. Coupled model for simulation of landslides and debris flows at local scale. *Nat. Hazards* 81, 1653–1682. <http://dx.doi.org/10.1007/s11069-016-2150-2>.
- Pastor, M., Stickle, M.M., Dutto, P., Mira, P., Merodo, J.A.F., Blanc, T., Sancho, S., Benitez, A.S., 2015. A viscoplastic approach to the behaviour of fluidized geomaterials with application to fast landslides. *Contin. Mech. Thermodyn.* 27 (1–2), 21–47.
- Pastor, M., Tayyebi, S.M., Stickle, M.M., Yagüe, A., Molinos, M., Navas, P., Manzanal, D., 2021. A depth integrated, coupled, two-phase model for debris flow propagation. *Acta Geotech.* <http://dx.doi.org/10.1007/s11440-020-01114-4>.
- Pastor, M., Yague, A., Stickle, M.M., Manzanal, D., Mira, P., 2017. A two-phase SPH model for debris flow propagation. *Numer. Anal. Methods Geomech.* 42 (3), 418–488. <http://dx.doi.org/10.1002/nag.2748>.
- Piton, G., Recking, A., 2016. Design of sediment traps with open check dams. I: Hydraulic and deposition processes. *J. Hydraulic Eng. (ASCE)* 142 (2), 04015045.
- Pudasaini, S., Hutter, K., Hsiau, S.-S., Tai, S.-C., Wang, Y., Katzenbach, R., 2007. Rapid flow of dry granular materials down inclined chutes impinging on rigid walls. *Phys. Fluids* 19, 053302.
- Rickenmann, D., 2005. Runout prediction methods. In: *Debris-Flow Hazards and Related Phenomena*. Praxis Springer, pp. 305–324.
- Rickenmann, D., Laigle, D., McArdell, B., Hübl, J., 2006. Comparison of 2D debris-flow simulation models with field events. *Comput. Geosci.* 10, 241–264. <http://dx.doi.org/10.1007/s10596-005-9021-3>.
- Ritter, A., 1892. Die fortplanzung der wasserwellen. *Z. Vereines Deutscher Ing.* 36, 947–954.
- Salciarini, D., Tamagnini, C., Conversini, P., 2010. Discrete element modelling of debris-avalanche impact on earthfill barriers. *Phys. Chem. Earth* 35, 172–181.
- Scheidt, C., Rickenmann, D., 2010. Empirical prediction of debris-flow mobility and deposition on fans. *Earth Surf. Processes Landforms* 35, 157–173. <http://dx.doi.org/10.1002/esp.1897>.
- Schraml, K., Thomschitz, B., McArdell, B., Graf, C., Kaitna, R., 2015. Modeling debris-flow runout patterns on two alpine fans with different dynamic simulation models. *Nat. Hazards Earth Syst. Sci. Discuss.* 3 (2), 1397–1425. <http://dx.doi.org/10.5194/nhess-15-1483-2015>.
- Solenthaler, B., Bucher, P., Chentanez, N., Müller, M., Gross, M., 2011. SPH-based shallow water simulation. In: *Workshop on Virtual Reality Interaction and Physical Simulation VRIPHYS (2011)*. pp. 1–8.
- Song, D., Zhou, G.G.D., Xu, M., Choi, C.E., Li, S., Zheng, Y., 2019. Quantitative analysis of debris-flow flexible barrier capacity from momentum and energy perspectives. *Eng. Geol.* 251, 81–92. <http://dx.doi.org/10.1016/j.enggeo.2019.02.010>.
- Stoker, J., 1957. *Water Waves*. Interscience.
- Teufelsbauer, H., Wang, Y., Chiou, M.-C., Wu, W., 2009. Flow-obstacle-interaction in rapid granular avalanches: DEM simulation and comparison with experiment. *Granul. Matter* 11 (4), 209–220.
- Tiberghien, D., Laigle, D., Naaim, M., Thibert, E., Ousset, F., 2007. Experimental investigation of interaction between mudflow and obstacle. In: Chen, C., Major, J.J. (Eds.), *Debris-Flow Hazards Mitigation: Mechanics, Prediction and Assessment*. pp. 281–292. <http://dx.doi.org/10.5334/jors.bl>.
- Vagnon, F., Segalini, A., Ferrero, A.M., 2015. Studies of flexible barriers under debris flow impact: an application to an alpine basin. *Procedia Earth Planet. Sci.* 15, 165–172. <http://dx.doi.org/10.1016/j.proeps.2015.08.041>.
- VanDine, D.F., 1996. Debris flow control structures for forest engineering. (Working Paper 08/1996), Res. Br., B.C. Min. For..
- Vela Vela, L., Reynolds-Barredo, J.M., Sánchez, R., 2019. A positioning algorithm for SPH ghost particles in smoothly curved geometries. *J. Comput. Appl. Math.* 353, 140–153. <http://dx.doi.org/10.1016/j.cam.2018.12.021>.
- Wang, Z., Shen, H., 1999. Lagrangian simulation of one-dimensional dam-break flow. *J. Hydraul. Eng.* 125 (11), 1217–1220.
- Whipple, K.X., Dunne, T., 1992. The influence of debris-flow rheology on fan morphology, Owens Valley, California. *Geol. Soc. Am. Bull.* 104, 887–900.